

Quantum Computation with Superconducting Parametric Cavity

by

Jimmy Shih-Chun Hung

A thesis
presented to the University of Waterloo
in fulfillment of the
thesis requirement for the degree of
Master of Applied Science
in
Electrical and Computer Engineering (Quantum Information)

Waterloo, Ontario, Canada, 2020

© Jimmy Shih-Chun Hung 2020

Author's Declaration

I hereby declare that I am the sole author of this thesis. This is a true copy of the thesis, including any required final revisions, as accepted by my examiners.

I understand that my thesis may be made electronically available to the public.

Abstract

Multimode superconducting parametric cavity is a flexible platform that has been used to study a variety of topics in microwave quantum optics ranging from parametric amplification, entanglement generation to higher order spontaneous parametric downconversion (SPDC). Leveraging the extensive toolbox of interactions available in this system, we can look to explore exciting applications in quantum computation and simulation. In this thesis, we study the use of the parametric cavity to realize continuous variable (CV) quantum computation.

We propose and examine in detail the scheme to compute with the microwave photons in the orthogonal frequency modes of the cavity via successive application of parametric pump pulses or cavity drives. The family of all Gaussian transformations can be accomplished easily with interactions already demonstrated in this system. From recent results and proposals involving higher order SPDC, there are also clear pathways towards realizing the non-Gaussian resources necessary for universal computation. Common measurements on the system are accomplished with standard measurement techniques on the output state of the cavity and additional useful measurements may be implemented using available parametric interactions or new device designs involving a qubit as a nonlinear probe.

Using the parametric cavity, we experimentally implemented a hybrid quantum-classical machine learning algorithm called the Quantum Kitchen Sinks (QKS) as the first step towards developing this platform for quantum computation. The algorithm is studied over two sets of experiments starting from partial experimental implementation of the quantum variational circuits to fully experimental implementation using multiple simultaneous continuous wave (CW) pumps. In both cases, we find that the quantum part of the algorithm implemented in the parametric cavity improved the classification accuracy on a difficult synthetic data set up to 90.1% and 99.5% respectively when compared to a classical linear machine learning algorithm.

Acknowledgements

It has been quite the enjoyable journey to step into this exciting field of research. Beyond the rewards of scientific pursuit, it is the excellent people who made the last two years the most fun I've had.

First and foremost, I would like to thank my advisor, Chris Wilson, for being the best mentor and role model. Chris's extensive knowledge and patience as a teacher is instrumental in helping me tackle new topics of research. In addition to the technical guidance, I learned a lot about the qualities and mindsets it takes to be a good scientist from working with Chris. I am grateful to Chris for providing the opportunities and encouragement to pursue a variety of projects and attend various conferences.

Next, I would like to extend special thanks to Sandbo, a past PhD student in EQSL who is a great friend and mentor. With infinite patience and willingness to help, Sandbo taught me every thing I know about all aspects of lab work. I am inspired daily by his curiosity, dedication and attention to details. It is always fun to discuss all things in life from computer parts to experimental results or just random ideas. And of course, the work in this thesis is only possible thanks to Sandbo's device and research on parametric interactions that laid the groundwork.

I would also like to thank the rest of my group members and friends at EQSL. Jamal is a great friend and I enjoy the countless hours we spent working together in lab, fabricating in cleanroom, and taking coffee breaks at Timmy's. Thanks to the fabrication expertise and help from Ibrahim and Vadiraj, I was able to take on the fabrication of a new device despite having no prior experience. I would like to thank the rest of EQSL members including Dima, Huichen, Mehran, Nizar and more. I am also grateful for the invaluable help I have received from cleanroom staff at QNFCF including Nathan, Paul, Greg, Matt, Rod and Brian.

Lastly, I am thankful for my partner, Lisa, for her love and encouragement throughout my degree.

Table of Contents

List of Figures	vii
List of Tables	ix
1 Introduction	1
1.1 Overview	2
2 Superconducting Parametric Cavity	4
2.1 Josephson Junctions	4
2.2 DC SQUID	6
2.3 Multimode Tunable Cavity	8
2.4 Parametric Interactions	11
2.5 Device	14
3 CV Quantum Computation in Parametric Cavity	16
3.1 Short Introduction to CV Quantum Computation	16
3.1.1 Gaussian states and gates	18
3.1.2 Universality	18
3.1.3 CV Computation Protocols	19
3.2 Quantum Computation with the Multimode Parametric Cavity	20
3.3 Gates	21

3.3.1	Gaussian Gates	21
3.3.2	Non-Gaussian Resources	25
3.3.3	Multitone Pumping	27
3.3.4	Summary of Gate Implementations	30
3.4	Measurements	32
3.4.1	Cavity Output Mode	32
3.4.2	Heterodyne Detection	33
3.4.3	Homodyne Detection	34
3.4.4	In-Situ Amplification	35
3.4.5	Fast Measurement of Cavity State	37
3.4.6	Photon Counting	37
4	Experimental Implementation of QKS Algorithm	41
4.1	Quantum Machine Learning and the Quantum Kitchen Sinks Algorithm . .	41
4.2	Experiment	43
4.2.1	Quantum Variational Circuit with the Parametric Cavity	44
4.2.2	Classical Components of QKS	44
4.2.3	Experiment Setup	46
4.2.4	Mixed Experiment/Simulation	49
4.2.5	CW Pump Experiment	51
4.2.6	Summary	52
5	Conclusion	53
5.1	Future Directions	54
	References	55

List of Figures

2.1	Josephson junction	5
2.2	DC SQUID	7
2.3	Tunable $\lambda/4$ cavity	9
2.4	CAD drawing of the parametric cavity	14
3.1	CV quantum computation on parametric cavity	20
3.2	Gaussian transformations	21
3.3	Trisqueezed state	26
3.4	Cubic phase state	27
3.5	Multimode entanglement	28
3.6	Multitone pumping	29
3.7	Measurement channel	32
3.8	Linear measurements	34
3.9	In-situ amplification	35
3.10	Two channel detection	36
3.11	Quantum teleportation	37
3.12	Device with qubit probe	39
4.1	Classification in feature space	42
4.2	Quantum Kitchen Sinks	43
4.3	Quantum variational circuit	44

4.4	Fisher linear discriminant	45
4.5	Experiment overview	46
4.6	Measurement setup	48
4.7	Mixed experiment/simulation	49
4.8	Mixed experiment/simulation results	50
4.9	CW pump experiment	51
4.10	CW pump experiment results	52

List of Tables

3.1	Summary of CV gates	31
3.2	Device parameters for a transmon qubit coupled to the parametric cavity .	39

Chapter 1

Introduction

The past few decades have been exciting for the field of quantum computation with the discovery of algorithms that promise significant speed-up and the development of many quantum computation platforms based on different physical systems. However, in order to achieve a practical and fault-tolerant quantum computer, many challenges still need to be addressed. Of the various systems actively studied in quantum computing, superconducting quantum circuit has become a well-established and leading platform for research in quantum computation due to its flexibility and potential for scaling. Many research groups and industry partners are tackling the challenges to implement a quantum computer using superconducting quantum circuits as the main platform.

The first step in implementing a quantum computation platform involves encoding quantum information in the properties of a chosen physical system. For example, in optical quantum computing, the information may be encoded in a discrete variable (DV) fashion using a photon's discrete spatial modes, such as its polarization or optical path [1]. A value of 1 or 0 may be represented by polarizing the photon in either the horizontal or vertical direction. Alternatively, the information can also be encoded in so-called continuous variable (CV) states, such as the electric field amplitude and phase [2]. These encoding schemes have their advantages and disadvantages, but they can all achieve universal quantum computation given an appropriate source of nonclassical light [3, 4].

In the realm of superconducting quantum computers, the dominant paradigm for quantum information encoding is to use the discrete energy levels of transmon qubits. Nonetheless, there are some efforts to consider CV systems in superconducting systems. For example, the “cat code” technique uses interaction between qubits and oscillator to encode quantum information in a type of CV state, a “cat” state, that can implement hardware-

efficient quantum error correction [5]. More recently with the advancements in quantum control of an oscillator, many more CV qubit encoding schemes have been realized experimentally, such as, the binomial code [6] and the Gottesman-Kitaev-Preskill code [7].

The majority of investigation in superconducting devices on quantum computation using CV states involves encoding logical qubits in these systems. Alternatively, instead of encoding a qubit, one can also consider quantum computation over continuous variables directly with the so-called qumodes. Traditionally more frequently explored in the optical domain, such schemes often involve linear optical elements acting on bosonic modes along with some non-Gaussian resources such as the single photon state or photon number resolution measurement. The superconducting parametric cavity offers an exciting opportunity to implement computation over continuous variables in the superconducting domain due to the rich toolbox of available interactions. Many transformations equivalent to linear optical elements as well as some novel non-Gaussian resources that cannot yet be achieved in the optical domain can be readily realized in this device. The superconducting parametric cavity is essentially like a single-chip optical table for microwave photons that comes with new components which opens up exciting new opportunities.

1.1 Overview

The goal of my research detailed in this thesis is to investigate and develop superconducting parametric cavities as an alternative computation platform based on CV states of microwave photons in cavities. Building upon recent work on two and three photon parametric interactions from colleagues in the Engineered Quantum Systems Laboratory (EQSL), we seek to characterize and harness these interactions along with other interactions to realize a complete framework for CV quantum computation. In parallel with the development of this computation platform, we also work towards the implementation of some simple quantum algorithms to demonstrate the capability of this platform for use in quantum computation. This thesis presents the first steps in our efforts towards these goals.

In chapter 2, we start by introducing the superconducting parametric cavity device explored in this thesis. The basic superconducting circuit building blocks are introduced along with a discussion of how parametric interactions are realized in this device. Additionally, important design details that enable us to use this device for computation are examined as well.

In chapter 3, we propose a scheme to realize CV quantum computation in this device. We then cover the realization and some initial characterization of various CV gates and

resource states in this device. We also discuss the requirement for universality as well as pathways to achieve it. Since measurement is another crucial part of quantum computation, the focus then moves to the discussion of the measurement channels and measurement schemes we can implement for this device. In addition, we also introduce some proposals to improve the measurement schemes using features of the device. Finally, we discuss other measurements that may be enabled by some design modifications and briefly introduce a new device design currently in the works.

In chapter 4, we detail the experimental implementation of the Quantum Kitchen Sinks (QKS) algorithm in our effort towards demonstrating the capability of the parametric cavity as a quantum computation device. We first discuss various components of the experiments from the classical part of algorithm to the specific implementation of the quantum part as well as the experimental setup. We then carry out two sets of experiments to demonstrate the algorithm and benchmark its performance.

Chapter 2

Superconducting Parametric Cavity

The device explored in this thesis is a superconducting parametric cavity consisting of an aluminum thin film coplanar waveguide (CPW) microwave resonator capacitively coupled to an open transmission line at one end and terminated by a flux-pumped SQUID at the other end. This chapter introduces the constituent elements of the device, principles behind flux-pumped parametric interactions, and finally notable design considerations that enable us to explore quantum computation with this device.

2.1 Josephson Junctions

Found in many applications from magnetometers to classical computation with single flux quantum logic and quantum computation with artificial atoms, Josephson junction is a simple device that is at the heart of superconducting circuits.

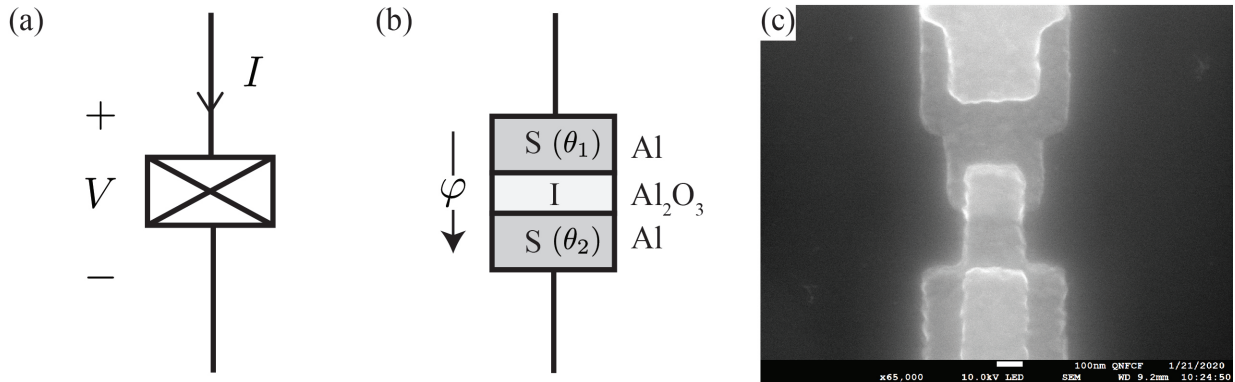


Figure 2.1: Josephson Junction. (a) Schematic symbol of a Josephson junctions. (b) Two pieces of superconducting Al thin films are separated by a thin insulating barrier made of Aluminum oxide. Cooper pairs can tunnel through the barrier as supercurrent which relates to the phase difference φ between the two superconductors. (c) An SEM image of a Josephson junction where the critical current I_c is lithographically defined by the overlap area of the Al layers.

Josephson junction consists of two pieces of superconductors coupled by a weak link such as a thin insulating barrier (see Fig. 2.1). For low temperature superconductors described by the BCS theory, such as Al, an effective attractive interaction between electrons of opposite spin mediated by phonons results in the formation of pairs of electrons called Cooper pairs in the material's superconducting phase [8]. The Cooper pairs form a condensate which can be described with a macroscopic wavefunction of the form

$$\Psi(\vec{r}, t) = \sqrt{n(\vec{r}, t)} e^{i\theta(\vec{r}, t)} \quad (2.1)$$

where $n(\vec{r}, t)$ is density of Cooper-pairs and $\theta(\vec{r}, t)$ is phase.

When two pieces of superconducting metal are separated by a thin insulating barrier, the wavefunctions have decaying but non-zero magnitude across the barrier resulting in non-zero probability for Cooper pairs to tunnel across the junction. The supercurrent across the Josephson junction that arises as a result of this is described by the two Josephson relations [9]

$$I = I_c \sin(\varphi) \quad (2.2)$$

$$V = \left(\frac{\hbar}{2e} \right) \frac{\partial \varphi}{\partial t} = \left(\frac{\Phi_o}{2\pi} \right) \frac{\partial \varphi}{\partial t} \quad (2.3)$$

where I_c is critical current of the junction and $\Phi_o = h/2e$ is the flux quantum and $\varphi = \theta_1 - \theta_2$ is the difference in phase of the two macroscopic wavefunction describing the Cooper-pair condensates in each piece of superconductor.

From the Josephson relations, one can consider the I-V characteristic of this device to see that it behaves like a nonlinear inductance

$$V = \left(\frac{\Phi_o}{2\pi I_c \cos \varphi} \right) \frac{\partial I}{\partial t} = L_J(\varphi) \frac{\partial I}{\partial t} \quad (2.4)$$

where the inductance $L_J(\varphi)$ depends nonlinearly on the phase difference across the junction. The energy stored in this device is

$$U(\varphi) = \int IV dt = -E_J \cos \varphi \quad (2.5)$$

where Josephson energy $E_J = U(0) = \frac{\Phi_o I_c}{2\pi}$ is a characteristic of the device based on design and fabrication. The nonlinearity of Josephson junctions coupled with negligible dissipation makes it a vital component in creating artificial atoms for quantum information processing and engineering interactions between microwave photons.

2.2 DC SQUID

A key element in superconducting parametric cavity is the DC superconducting quantum interference device (SQUID). It is a device formed by two Josephson junctions connected in a loop. See Fig. 2.2. The device couples the magnetic flux threaded through the loop to phase difference across the Josephson junctions. The SQUID acts effectively as a flux-tunable nonlinear inductive element which has applications in creating frequency tunable devices as well as realizing parametric interactions by fast flux modulation.

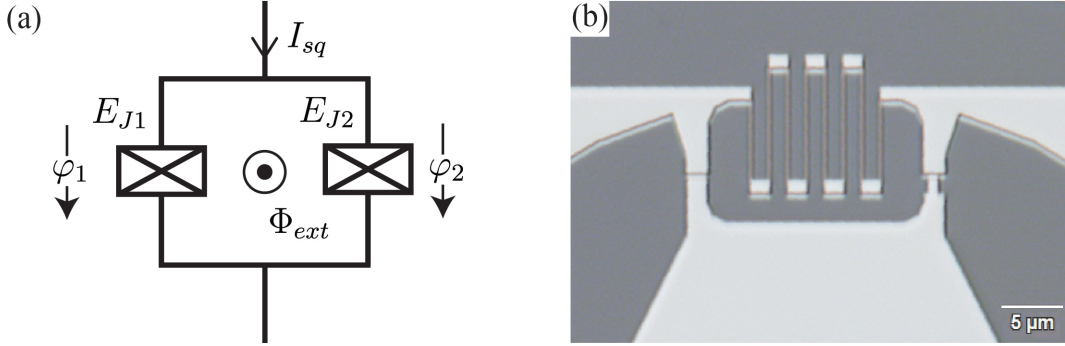


Figure 2.2: DC SQUID. (a) Circuit diagram of DC SQUID. (b) Optical microscope image of a SQUID with junctions of different E_J .

In the presence of a magnetic field and where current density $\vec{J} = 0$, the gradient of the macroscopic wavefunction phase can be related to the magnetic vector potential \vec{A} as $\nabla\theta = \frac{2\pi}{\Phi_o}\vec{A}$ [8]. Consider a loop Γ deep within the superconductor such that $\vec{J} = 0$ along the path, we can find the loop integral of phase gradient to be

$$\oint_{\Gamma} \nabla\theta \cdot d\vec{l} = \frac{2\pi}{\Phi_o} \oint_{\Gamma} \vec{A} \cdot d\vec{l} + \varphi_1 - \varphi_2 = 2\pi \frac{\Phi_{ext}}{\Phi_o} + \varphi_1 - \varphi_2 \quad (2.6)$$

where φ_1 and φ_2 are the phases across the two Josephson junctions. The loop integral of vector potential is also related to the magnetic flux threaded through the loop. Similar to fluxoid quantization argument, we require that the loop integral of phase gradient be integer multiple of 2π for the phase of the macroscopic wavefunction to be single-valued. As such, we find that

$$2\pi \frac{\Phi_{ext}}{\Phi_o} + \varphi_1 - \varphi_2 = 2\pi n, \quad n \in \mathbb{Z} \quad (2.7)$$

In the regime where $n = 0$, this connects the external flux threading the SQUID to the phase difference between the two Josephson junctions as

$$\varphi_2 - \varphi_1 = 2\pi \frac{\Phi_{ext}}{\Phi_o} \quad (2.8)$$

Now, by charge conservation or Kirchoff's current law, the total current passing through the SQUID I_{sq} can be written in terms of phases of individual junctions as

$$I_{sq} = I_1 + I_2 = I_{c1} \sin(\varphi_1) + I_{c2} \sin(\varphi_2) \quad (2.9)$$

For simplicity, let us first consider symmetrical SQUID with the same junction on either side of the loop such that $I_{c1} = I_{c2} = I_c$, then the SQUID current can be expressed as

$$I_{sq} = 2I_c \cos\left(\frac{\varphi_2 - \varphi_1}{2}\right) \sin\left(\frac{\varphi_2 + \varphi_1}{2}\right) = 2I_c \cos\left(\pi \frac{\Phi_{ext}}{\Phi_o}\right) \sin(\varphi_{sq}) \quad (2.10)$$

where the phase across the SQUID is defined to be $\varphi_{sq} = \frac{\varphi_1 + \varphi_2}{2}$.

Comparing Eq. (2.10) to Eq. (2.2), the SQUID essentially resembles JJ with critical current that is tunable via externally applied flux where the flux-tunable critical current is

$$I_{c,sq}(\Phi_{ext}) = 2I_c \cos\left(\pi \frac{\Phi_{ext}}{\Phi_o}\right) \quad (2.11)$$

The effective inductance of the SQUID can similarly be derived to be

$$L_{sq}(\varphi_{sq}, \Phi_{ext}) = \frac{\Phi_o}{2\pi I_{c,sq}(\Phi_{ext}) \cos \varphi_{sq}} = \frac{1}{2} \left(\frac{\phi_o}{2\pi I_c} \right) \left(\frac{1}{\left| \cos\left(\pi \frac{\Phi_{ext}}{\Phi_o}\right) \right| \cos(\varphi_{sq})} \right). \quad (2.12)$$

2.3 Multimode Tunable Cavity

The other main element in this device are microwave resonators which can be tuned and modulated by external flux. Microwave resonators can be realized in many ways such as with lumped element inductor and capacitor or as a cavity where a microwave waveguide is terminated by reflective boundary conditions. Here we consider a 1D microwave cavity composed of coplanar waveguide (CPW) terminated at one end with a low impedance element shunting the centre conductor to ground. The other end of the waveguide is connected to an output transmission line via a capacitor acting as a semi-reflective mirror. This is commonly known as the $\lambda/4$ transmission line resonator where the length of the transmission line is a quarter of the fundamental mode wavelength.

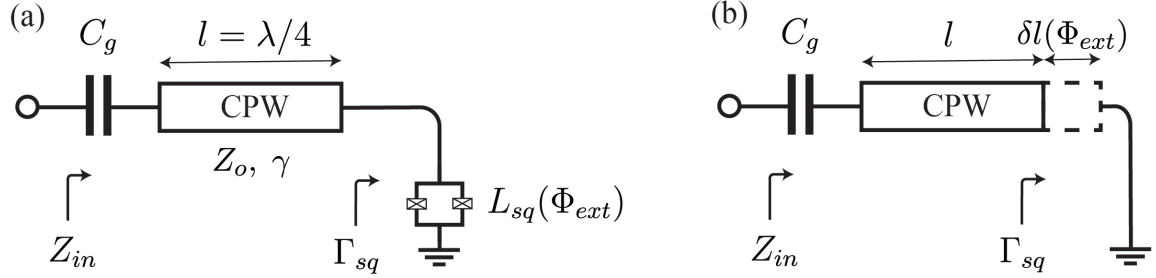


Figure 2.3: Tunable $\lambda/4$ cavity. (a) A tunable CPW transmission line resonator where the length of the transmission line is a quarter of the fundamental mode wavelength. The resonator is coupled externally via capacitor C_g and terminated by a small tunable inductance L_{sq} from the SQUID. (b) The tunable inductive boundary condition can be equivalently seen as an additional tunable electrical length before a short circuit.

First let us consider the resonant frequencies of a regular capacitively coupled $\lambda/4$ transmission line cavity. Here we consider a circuit similar to one shown in Fig. 2.3 (a) but with the SQUID side directly shorted to ground. A transmission line is characterized by its characteristic impedance Z_o and complex propagation constant $\gamma = \alpha + j\beta$ where α is the per unit length attenuation constant and $\beta = 2\pi/\lambda = \omega\sqrt{\epsilon_{eff}}/c$ is the phase change per unit length. ϵ_{eff} is the effective dielectric constant for the propagating mode of the transmission line. The input impedance Z_{in} of the resonator can be found by the impedance of series connected capacitor summed with the impedance transformation of the short circuit boundary condition $Z_L = 0$ across transmission line of length l . For simplicity, we consider lossless case where $\alpha = 0$.

$$Z_{in}(\omega) = \frac{1}{j\omega C_g} + Z_o \frac{Z_L + Z_o \tanh \gamma l}{Z_o + Z_L \tanh \gamma l} = j \left(-\frac{1}{\omega C_g} + Z_o \tan \beta l \right) \quad (2.13)$$

Resonance occurs when the input impedance is purely real [10]. We can therefore find the resonance frequency by solving the following transcendental equation.

$$\text{Im}(Z_{in}(\omega)) = -\frac{1}{\omega C_g} + Z_o \tan \beta l = 0 \quad (2.14)$$

In the limit of small external coupling $C_g \rightarrow 0$ or the case of unloaded resonator, resonances occur when $\beta l = \pi(1/2 + m)$. The resonance frequency of m th mode is

$$f_m = f_0(1 + 2m) \quad (2.15)$$

$$f_0 = \frac{c}{4\sqrt{\epsilon_{eff}}l} \quad (2.16)$$

where $m \in \mathbb{N}$ and f_0 is the fundamental mode frequency. In short, the $\lambda/4$ resonator supports multiple resonant modes that are all roughly separated by $2f_0$ in frequency. The mode frequencies in practice are never perfectly evenly spaced due to various frequency dependent effects ranging from impedance of output coupling element to load impedance.

To make this cavity tunable, instead of shorting one end of the waveguide to ground, it is instead shunted by a SQUID which can be considered a flux-tunable inductance. See Fig. 2.3 (a). One can follow the same procedure as in Eq. (2.13) with the appropriate Z_L of the SQUID to determine the input impedance and thus the resonant frequency of the SQUID terminated $\lambda/4$ resonator. To more effectively illustrate the effect of the SQUID on resonance frequencies, first consider the impedance of a symmetric SQUID modelled as a tunable inductor. We assume small φ_{sq} here to linearize the nonlinear inductance.

$$Z_{sq}(\Phi_{ext}) = j\omega L_{sq}(\Phi_{ext}) = j\omega \frac{L_{sq,min}}{\left| \cos\left(\pi \frac{\Phi_{ext}}{\Phi_o}\right) \right|} \quad (2.17)$$

where $L_{sq,min} = \frac{\Phi_o}{4\pi I_c}$ is the minimum SQUID inductance at $\Phi_{ext} = 0$. As we sweep the external flux from 0 to $\Phi_o/2$, the inductance and therefore the reactance increases from a minimum to infinity or equivalently an open circuit. For an incident wave V^+ on the SQUID, the reflected wave V^- always has equal magnitude but acquires a phase shift ϕ dependent on the value of the inductance that ranges from close to π in the case of small minimum inductance to 0 in the case of maximum inductance or equivalently open circuit. This is to say that the reflection coefficient is

$$\Gamma_{sq}(\Phi_{ext}) = \frac{V^-}{V^+} = \frac{Z_{sq}(\Phi_{ext}) - Z_o}{Z_{sq}(\Phi_{ext}) + Z_o} = e^{j\phi(\Phi_{ext})} \quad (2.18)$$

As illustrated in Fig. 2.3 (b), this acquired phase shift in the reflection from tuning the SQUID with flux is equivalent to moving a short circuit boundary condition closer or further away – effectively shortening or lengthening the cavity.

Finally, we need to consider the coupling of the cavity through the capacitor to an external load such as the measurement chain. While for most of the analysis so far we have assume the cavity to be lossless, in practice there are still various loss mechanisms in the resonator including substrate dielectric losses, losses at interfaces and surfaces, and coupling to stray two-level systems [11]. The internal losses of the resonator is captured in the internal quality factor Q_i which is typically above $\approx 50,000$ for our SQUID terminated $\lambda/4$ cavity. The coupling of excitation in the cavity to the external load through the coupling capacitor C_g defines the external quality factor Q_e . The external quality factor

can be numerically derived from the input reflection coefficient which is found in a similar way as Eq. (2.13) where we transform effect of the load down the transmission line. The device is designed to be overcoupled to the external load such that $Q_e < Q_i$. In this case, the external coupling is the dominant loss channel so most of the photons in the cavity are lost to the measurement chain instead of through other loss mechanisms that do not contribute to the measurement process.

2.4 Parametric Interactions

In section 2.3, the ability to tune the resonant frequencies of cavity modes through external magnetic flux threading the SQUID is introduced. In typical operation, the resonant frequencies are tuned to certain set points with static magnetic field generated by a DC coil attached to the sample holder. In addition to the DC magnetic flux, there is also an on-chip fast-flux line that allows us to introduce fast-oscillating flux to the SQUID which drives the parametric processes.

Following the derivations in [12, 13, 14], we can show how the parametric interactions between modes are realized in a SQUID-terminated cavity. Ignoring parasitic capacitance of the Josephson junctions, the Hamiltonian of a symmetric SQUID consisting of junctions with Josephson energy E_J is

$$\hat{H}_{sq} = 2E_J \left| \cos \left(\pi \frac{\hat{\Phi}_{ext}}{\Phi_o} \right) \right| \cos \left(2\pi \frac{\hat{\Phi}_c}{\Phi_o} \right) \quad (2.19)$$

Here we used a change of variable from the phase across the SQUID φ_{sq} to the node flux Φ_c . The node flux variable commonly used in cQED is defined in relation to the voltage at a node as $\Phi = \int_{t_0}^t d\tau V(\tau)$. From the second Josephson equation in Eq. (2.3), the node flux across Josephson junction at one end of the cavity is related to phase across the junction as $\varphi = 2\pi\Phi/\Phi_o$.

The node flux at some point along the cavity is related to the normal mode flux Φ_k and spatial profile u_k of the cavity modes as $\Phi(x, t) = \sum_{k=0}^{\infty} u_k(x)\Phi_k(t)$. In the quantum treatment of transmission line cavity resonances, the cavity modes are quantized and the flux of each mode $\hat{\Phi}_k$ is proportional to the bosonic annihilation \hat{a}_k and creation \hat{a}_k^\dagger operators of the mode $\hat{\Phi}_k \propto \hat{a}_k + \hat{a}_k^\dagger$ [11]. The node flux across the SQUID $\hat{\Phi}_c$ is thus some linear combination of all the cavity modes creation and annihilation operators. Now we also consider both static and fast-oscillating parts of the externally threaded flux as $\hat{\Phi}_{ext} =$

$\Phi_{DC} + \hat{\Phi}_p$ where Φ_{DC} is the static flux bias from the DC coil and $\hat{\Phi}_p$ is the pump signal injected through the fast flux line.

Expanding cosines in Eq. (2.19) to first order of $\hat{\Phi}_p$ around Φ_{DC} and to second order of $\hat{\Phi}_C$, the approximate Hamiltonian ignoring some constant factors for purpose of illustration shown below

$$\hat{H}_{sq} \approx \hbar g_o (\hat{a}_p + \hat{a}_p^\dagger) \left(\sum_{k=0}^{\infty} \hat{a}_k + \hat{a}_k^\dagger \right)^2 \quad (2.20)$$

The cosine nonlinearity involving the cavity flux $\hat{\Phi}_c$ gives rise to quadratic cross terms between the creation and annihilation operators of the cavity modes. Due to the even nature of the cosine function, we only have even power terms in the expansion. Now, the Hamiltonian of the system considering the energy of the cavity modes and pump field in addition to the small modulation of SQUID energy is

$$\begin{aligned} \hat{H} &= \hat{H}_o + \hat{H}_{sq} \\ &= \hbar \omega_p \hat{a}_p^\dagger \hat{a}_p + \sum_{k=0}^{\infty} \hbar \omega_k \hat{a}_k^\dagger \hat{a}_k + \hat{H}_{sq} \end{aligned} \quad (2.21)$$

Moving to the interaction picture with the unitary transformation $\hat{U}_o = e^{\frac{i}{\hbar} \hat{H}_o t}$, the interaction Hamiltonian is

$$\begin{aligned} \hat{H}_{int} &= i\hbar \dot{\hat{U}}_o \hat{U}_o^\dagger + \hat{U}_o \hat{H} \hat{U}_o^\dagger = \hat{U}_o \hat{H}_{sq} \hat{U}_o^\dagger \\ &= \hbar g_o (\hat{a}_p e^{-i\omega_p t} + \hat{a}_p^\dagger e^{i\omega_p t}) \left(\sum_{k=0}^{\infty} \hat{a}_k e^{-i\omega_k t} + \hat{a}_k^\dagger e^{i\omega_k t} \right)^2 \end{aligned} \quad (2.22)$$

where the annihilation and creation operators acquire a time dependency in phase $\hat{a}_k \rightarrow \hat{a}_k e^{-i\omega_k t}$. Since the pump tone is a strong coherent tone, we can apply the parametric approximation $\hat{a}_p \rightarrow |\alpha_p| e^{-i\theta_p}$ where the operator is replaced with the classical amplitude $|\alpha_p|$ and phase θ_p . In the interaction picture, different cross terms has different frequency dependencies. We can selectively activate the interactions of interest by setting the pump frequency resonant to the terms of interest. For instance, if we would like to activate coherent coupling between two modes, we set the pump frequency to be the difference frequency between the two modes $\omega_p = |\omega_2 - \omega_1|$. Looking only at two modes, the interaction Hamiltonian is

$$\hat{H}_{int} = \hbar g_o |\alpha_p| \left(e^{i\theta_p} \hat{a}_1^\dagger \hat{a}_2 + e^{-i\theta_p} \hat{a}_2^\dagger \hat{a}_1 \right) + \hat{H}_{rot}(t) \quad (2.23)$$

where we have a static term and other fast oscillating terms in \hat{H}_{rot} . With rotating wave approximation, we can ignore the effect of the fast oscillating terms as the effects would quickly average out, leaving us with the desired coherent coupling interaction

$$\hat{H}_{CC} = \hbar g_o |\alpha_p| \left(e^{i\theta_p} \hat{a}_1^\dagger \hat{a}_2 + e^{-i\theta_p} \hat{a}_2^\dagger \hat{a}_1 \right). \quad (2.24)$$

Notice here that the pump amplitude and phase gives us control over the interaction strength $g = g_o |\alpha_p|$ as well as the well defined phase θ_p of the interaction. This ability to create coherent coupling between arbitrary modes of the system with well defined phase proves to be particularly useful in our other work on quantum simulation of lattice models under magnetic field [15].

The example so far illustrates how quadratic interactions in this system are achieved with parametric pumping of a symmetric SQUID. From Eq. (2.19), it is evident that the expansion of the cavity flux $\hat{\Phi}_c$ only has even order terms as cosine is an even function. To achieve cubic interactions such as three-photon spontaneous parametric down conversion (SPDC), there needs to be some odd order expansion involving the cavity flux. This is achieved through making the SQUID junctions asymmetric where $E_{J1} \neq E_{J2}$. See Fig. 2.2 (b). From [14], the Hamiltonian of an asymmetric SQUID is

$$\hat{H}_{sq} = E_J(\hat{\Phi}_{ext}) \cos \left(2\pi \frac{\hat{\Phi}_c}{\Phi_o} - \alpha(\hat{\Phi}_{ext}) \right) \quad (2.25)$$

$$E_J(\hat{\Phi}_{ext}) = \sqrt{E_{J,1}^2 + E_{J,2}^2 + 2E_{J,1}E_{J,2} \cos \left(2\pi \frac{\hat{\Phi}_{ext}}{\Phi_o} \right)} \quad (2.26)$$

$$\alpha(\hat{\Phi}_{ext}) = \arctan \left[\tan \left(\pi \frac{\hat{\Phi}_{ext}}{\Phi_o} \right) \frac{E_{J,1} - E_{J,2}}{E_{J,1} + E_{J,2}} \right] \quad (2.27)$$

where we still have an external flux tunable E_J of the SQUID as well as a external flux dependent bias α in the cavity flux cosine term. α comes from the asymmetry between the SQUID junctions as shown in Eq. (2.27) and gives the desired odd order terms in expansion of the cavity flux term. With similar resonant selection by the choice of pump frequency, we can parametrically activate interactions of interest such as three photon SPDC $\hbar g(\hat{a}_1^\dagger \hat{a}_2^\dagger \hat{a}_3^\dagger + \hat{a}_1 \hat{a}_2 \hat{a}_3)$ or the 1-to-2 photon conversion $\hbar g(\hat{a}_1^\dagger \hat{a}_2 \hat{a}_2 + \hat{a}_1 \hat{a}_2^\dagger \hat{a}_2)$.

2.5 Device

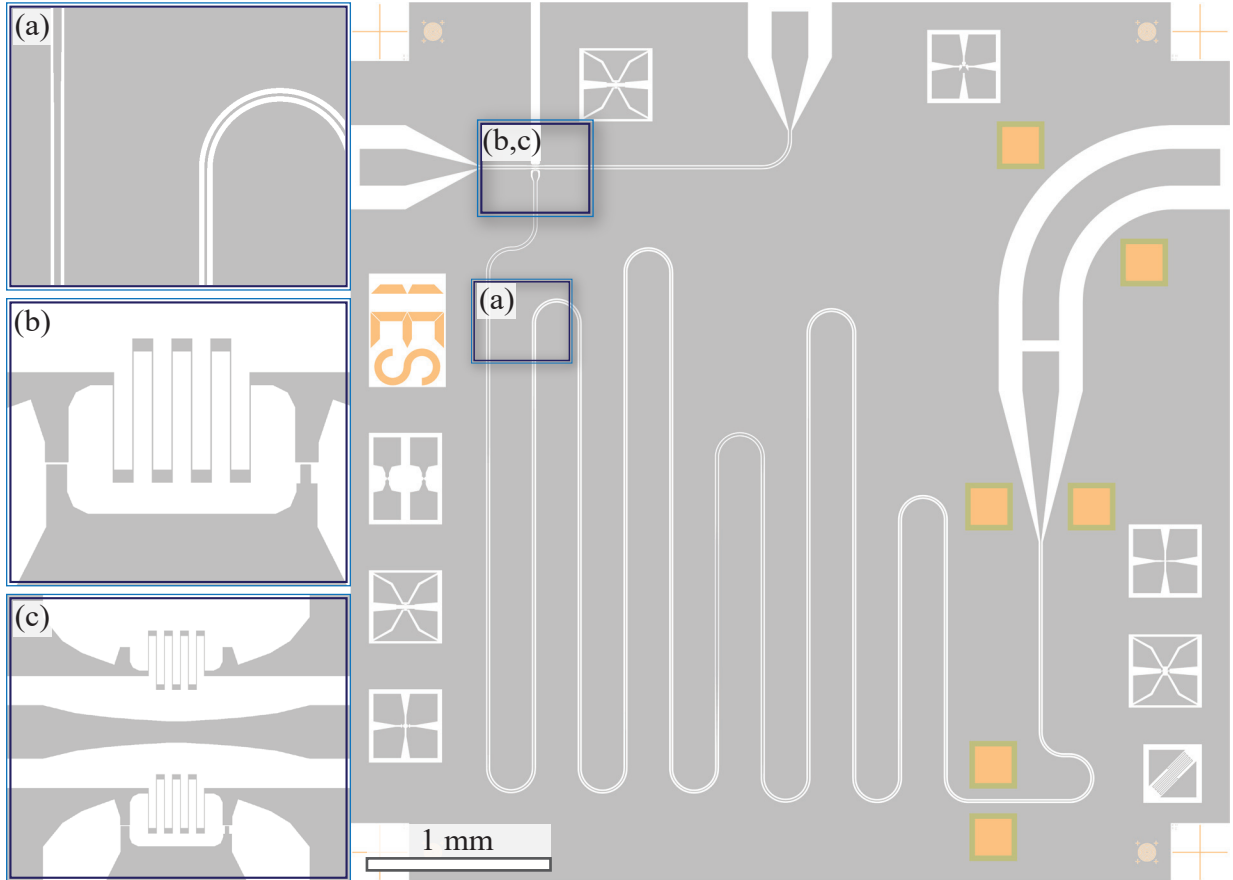


Figure 2.4: CAD drawing of the parametric cavity designed by Sandbo Chang. (a) Transmission line characteristic impedance is modulated along the cavity by altering the width of the centre conductor. This impedance modulation give rise to non-degenerate frequency spacings. (b) SQUID is composed of asymmetric junctions which gives us access to third order interactions between cavity modes. (c) Ground current of the pump line directly couples to the SQUID through kinetic inductance from a thin meandering structure.

The device used to conduct the experiments in this thesis was designed and fabricated by Chung Wai Sandbo Chang [12](see Fig. 2.4). Originally designed as a source for generating propagating quantum states of microwave, Chang achieved the generation of multimode entangled microwaves [13], the application of entangled microwaves for quantum illumination

[16], and the first observation of direct three-photon SPDC [14]. These experiments and the engineering of the device by Chang paved the way for further applications of this device in the context of a quantum information processing device rather than a quantum microwave source. The flexible and controllable parametric interactions enabled by Chang’s design allows us to explore this device as a programmable analog quantum simulator and as a continuous variable quantum computer in the case of this thesis.

The $\lambda/4$ coplanar waveguide resonator is patterned on an electron-beam evaporated Al thin film on intrinsic Si substrate using standard electron-beam and optical lithography techniques. The cavity is overcoupled to an output 50Ω transmission line via an approximately 16 fF gap capacitor which gives a measured Q of around 7000 for the 4 GHz mode. The cavity length is chosen to be long enough such that the fundamental mode is at approximately 1 GHz which gives us access to around 4 or 5 modes within our typical measurement bandwidth of 4 to 12 GHz.

For the most part this device resembles a typical SQUID terminated $\lambda/4$ resonator, but there are three key design details that enable us to use this device for computation. The first being the engineering of cavity mode frequencies in a way such that the frequency spacings are non-degenerate. This means that interactions that would typically be activated by parametric pumps of the same frequency, such as coherent coupling between successive modes, can now be individually addressed with different pump frequencies. This is achieved through impedance modulation of the $\lambda/4$ line where Chang split the transmission line into 12 sections of different characteristic impedance and joins the sections with short CPW tapers (see Fig. 2.4 (a)). The second design detail is the SQUID asymmetry which gives us access to three-photon parametric interactions as introduced in section 2.4. This device has an asymmetry of 1:1.7 defined by a difference in junction overlap width (see Fig. 2.4 (b)).

Finally, the coupling of pump signal to SQUID is enhanced by the use of kinetic inductance in the ground path of the pump line in order to efficiently achieve stronger third order interaction strengths. One way to improve the pump coupling would be to increase the area of the SQUID loop thereby increasing flux threading the loop. However, this comes with the disadvantage of stronger coupling to flux noise from the environment which is detrimental to the coherence of the system. In this design, an additional kinetic inductance arising from kinetic energy of Cooper pairs in a thin superconductor is placed in the SQUID loop along the path travelled by the ground current of the pump line (see Fig. 2.4 (c)). This directly couples the pump signal into the loop integral of the condensate phase gradient and thus improves pump coupling by roughly 30 dB in comparison to designs without the kinetic inductance [14].

Chapter 3

CV Quantum Computation in Parametric Cavity

The multimode parametric cavity device described in Chapter 2 turns out to be a flexible platform to explore microwave quantum optics due to the scalability in the number of bosonic modes and the wide variety of interactions between these modes achievable via parametric modulation of the SQUID. Continuous variable (CV) quantum computation is natural to explore on this bosonic platform as many of the common transformations in CV protocols such as squeezing ($\hat{a}_1^\dagger \hat{a}_2^\dagger + \hat{a}_2 \hat{a}_1$) and beamsplitter ($\hat{a}_1^\dagger \hat{a}_2 + \hat{a}_2^\dagger \hat{a}_1$) interactions are straightforward to implement. Some higher order non-Gaussian interactions not yet demonstrated in other physical systems, such as direct 3-photon SPDC, present further exciting possibilities to achieve important CV resources like the cubic phase state. In this chapter, we introduce our proposal to use the multimode parametric cavity as a CV quantum computation platform.

3.1 Short Introduction to CV Quantum Computation

A CV quantum system is one that has an infinite-dimensional Hilbert space with observables or quantum operators that can be continuous in nature, such as the position and momentum of an oscillator. A basic type of CV system is the harmonic oscillator that describes many common physical systems including the resonant modes of electromagnetic

field in the parametric cavity. The hamiltonian of a single harmonic oscillator is

$$\hat{H} = \hbar\omega \left(\hat{a}^\dagger \hat{a} + \frac{1}{2} \right) \quad (3.1)$$

In place of the Pauli operators $(\hat{\sigma}_x, \hat{\sigma}_y, \hat{\sigma}_z)$ which describe a qubit, the relevant operators for the quantum harmonic oscillator are the bosonic mode annihilation and creation operators $(\hat{a}, \hat{a}^\dagger)$ and the quadrature field operators describing the position and momentum (\hat{q}, \hat{p}) . Taking the convention of setting $\hbar = 1$, these unitless quadrature operators relate to the bosonic mode operators as

$$\begin{aligned} \hat{q} &= (\hat{a} + \hat{a}^\dagger)/\sqrt{2} \\ \hat{p} &= -i(\hat{a} - \hat{a}^\dagger)/\sqrt{2}. \end{aligned} \quad (3.2)$$

In the parametric cavity, the unitless quadrature operators relate by some scaling factors to the pairs of physical continuous observables such as the voltage and current or the charge and flux of the resonant modes.

Much like the case of computation with qubits where one performs single and multi qubit transformations to manipulate the information encoded in a collection of N qubits, quantum information in the CV paradigm is encoded in a collection of N harmonic oscillators where each harmonic oscillator is called a qumode. Similarly, single and multi qumode transformations are performed to manipulate the quantum state. The system is described by a collection of bosonic mode operators $\{\hat{a}_i, \hat{a}_i^\dagger\}_{i=0}^N$ and quadrature operators $\{\hat{q}_i, \hat{p}_i\}_{i=0}^N$ satisfying the commutation relationships

$$\begin{aligned} [\hat{a}_i, \hat{a}_j^\dagger] &= \delta_{ij} \\ [\hat{q}_i, \hat{p}_j] &= i\delta_{ij}. \end{aligned} \quad (3.3)$$

The Bloch sphere is a useful visualization of a qubit where any state of a qubit lies in or on the Bloch sphere as a point. In a CV system, the Wigner function is one of the many ways to represent the state of a qumode. The Wigner function $W(q, p)$ is a quasiprobability distribution in the phase space (quadrature space) that fully represent any pure and mixed state of a qumode. The Wigner function of a density matrix $\hat{\rho}$ is defined as

$$W(q, p) = \frac{1}{4\pi^2} \iint \text{Tr} [\hat{\rho} e^{-iu\hat{q}-iv\hat{p}}] e^{iu\hat{q}+iv\hat{p}} dudv \quad (3.4)$$

3.1.1 Gaussian states and gates

Gaussian states are a class of quantum states in CV that by definition has Wigner functions that are Gaussian and is therefore completely characterized by the first two moments of the quadrature operators [17]. Gaussian states and their manipulation are of particular interests as many common states falls in this category including vacuum, coherent, squeezed and thermal states. Gaussian gates are unitary transformations that transform Gaussian states to Gaussian states and are generated by Hamiltonians that are up to quadratic order in the bosonic mode operators [2]. Transformations in this class includes one and two mode squeezing as well as those achieved by linear optical elements such as phase rotation, displacement and beamsplitting.

Gaussian states and gates are central to many CV computation protocols and are generally the most commonly available elements in many physical systems. However, Gaussian states and gates alone are insufficient for classically intractable computation. A purely Gaussian process can be efficiently simulated on a classical computer much like the case of qubit based computation with only gates from the Clifford group [18].

3.1.2 Universality

In the case of discrete variable systems, a quantum computer is universal if it is capable of approximating any unitary to arbitrary accuracy [19]. While one can encode a logical qubit into a CV system and compute over a discrete variable space, here we consider a system to compute directly over the infinite Hilbert space to implement algorithms such as CV versions of the Grover search [20] and Deutch-Jozsa algorithm [21]. In considering an infinite Hilbert space, the definition of universality needs to be more constrained. Lloyd and Braunstein defines universality in a CV quantum computer as the ability to approximate any transformation that is polynomial in the bosonic mode operators to arbitrary precision in finite steps [4].

As mentioned earlier, a purely Gaussian process can only achieve Gaussian states. In order to achieve universality, some non-Gaussian states or transformations are necessary and are therefore considered a resource in the system. To promote a purely Gaussian system to universality, it suffices to have a non-Gaussian resource that is of cubic order or higher [4]. A non-Gaussian resource state of particular interest is the cubic phase state $|\gamma\rangle$ generated by the action of cubic phase gate $V(\gamma)$ on an ideally infinitely squeezed vacuum state such as the zero momentum eigenstate $|0\rangle_p$

$$|\gamma\rangle = V(\gamma) |0\rangle_p = e^{i\gamma\hat{q}^3} |0\rangle_p \quad (3.5)$$

where γ is the cubicity. While there are many proposals to generate the cubic phase state via nonlinearities such as photon subtraction, photon number measurements or higher order parametric downconversion, there has been no experimental demonstration of the cubic phase state so far.

3.1.3 CV Computation Protocols

Since the first proposal of CV quantum computation by Lloyd and Braunstein using Gaussian transformations along with a non-Gaussian resource [4], there are many more proposals of computations both universal and not universal in the realm of CV. One computation protocol is the one-way quantum computation (1WQC) with CV cluster states. Also known as measurement-based quantum computation, 1WQC is different from the typical circuit model of quantum computing in the sense that the complexity of computation is moved from the successive gates that prepare and evolve the quantum states to a highly entangled initial state and a sequence of adaptive local measurements. The CV version of 1WQC uses multimode squeeze state or the so-called Gaussian cluster state as a resource along with homodyne measurements to achieve arbitrary Gaussian transformation [22]. With an addition of a single non-Gaussian resource state or measurement, the 1WQC with Gaussian cluster state can be universal as well.

Another well known protocol is Gaussian Boson sampling (GBS) which is an adaptation of Boson sampling protocol to use squeezed states as the resource instead of single photon Fock states [23]. GBS consists of interfering the input squeezed and vacuum states with a network of beamsplitters and rotation gates before sampling the output in the Fock basis. While GBS is not universal in terms of computation, it finds application in solving many relevant hard and possibly classically intractable problems including simulation of molecular vibronic spectra [24] and various graph problems [25, 26, 27].

More recently, with the development of the field of quantum machine learning, there has also been various proposals for quantum machine learning algorithms that can be implemented on CV systems. Some relevant proposals include CV quantum neural networks [28], Gaussian quantum reservoir computing [29], and various quantum-classical hybrid algorithms like machine learning with quantum kernels [30] and Quantum Kitchen Sinks [31]. The hybrid algorithms are of particular interest as they seek quantum enhancement by leveraging the limited quantum processing capability of currently available noisy, intermediate-scale quantum (NISQ) computers with the help of classical computation.

3.2 Quantum Computation with the Multimode Parametric Cavity

In the following sections, we introduce our proposal to use the multimode parametric cavity as a CV quantum computer starting with the overview of the computation scheme followed more detailed descriptions of various aspects such as gates and measurements in this system.

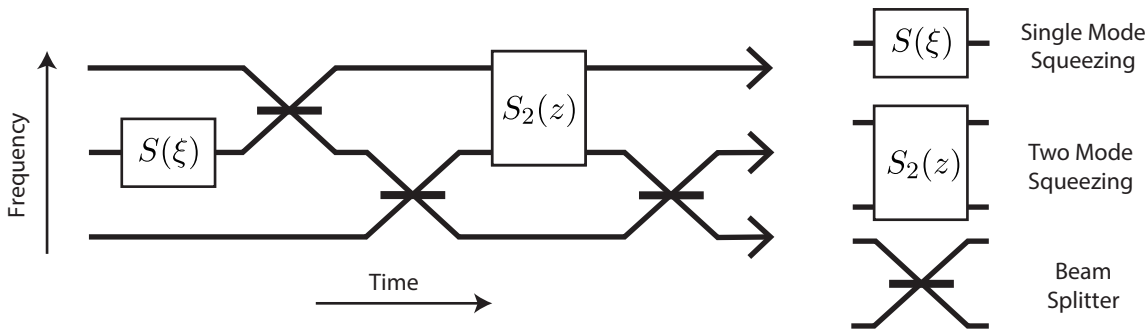


Figure 3.1: CV quantum computation on parametric cavity. Orthogonal frequency modes of the multimode cavity are the qumodes of the system and gates are implemented as successive parametric pump pulses or drive on the cavity.

Figure 3.1 illustrates the process to compute with the multimode parametric cavity. The orthogonal frequency modes of the cavity are the basis or qumodes in the CV quantum computer. In the cryogenic environment, the initial states of the qumodes are vacuum states or thermal states with low average photon number. Transformations on the qumodes are achieved either by successive application of parametric pump pulses to the SQUID to activate the desired interactions or by driving the cavity through the coupling capacitor. In the current parametric cavity design, the qumodes are finally measured by coupling the cavity state to an output transmission line via the coupling capacitor then measuring the output propagating state appropriately. With some modifications to the design, we can also envision expanding the measurement capability by methods such as parametric coupling to low Q modes for faster readout or dispersively coupling a transmon qubit to the cavity as a nonlinear probe which enables parity and photon number measurement of the cavity state.

The flexibility of parametric interactions in this cavity presents advantages like in-line squeezing as well as exciting opportunities such as the efficient generation of multimode

entanglement by simultaneous parametric pumping and the generation of the cubic phase state from trisqueezed state. While the asymmetric SQUID is the centrepiece to this system and presents many opportunities, the undesirable nonlinearity introduced by the SQUID even in the absence of parametric pumps may very well be a limiting factor of this system.

3.3 Gates

As mentioned in section 3.1.2, to achieve universality, it suffices to have the capability to generate all Gaussian transformations as well as a single non-Gaussian transformation of polynomial degree 3 or higher in the quadrature operator.

3.3.1 Gaussian Gates

Any Gaussian gate can be decomposed into a combination of displacement $D(\alpha)$, rotation $R(\phi)$, squeezing $S(r)$ and any two-mode transformations [2]. Here we outline the implementation of this set of gates in the parametric cavity.

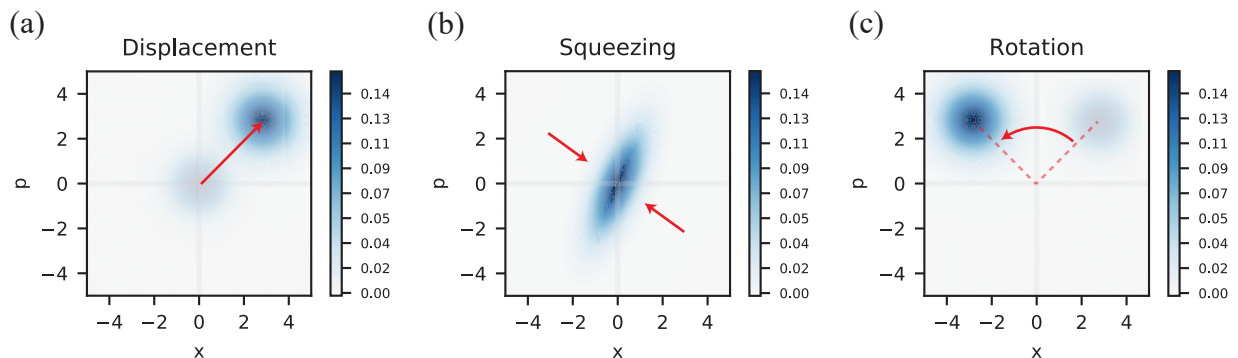


Figure 3.2: Action of common Gaussian transformations. Wigner function of (a) displacement acting on vacuum to create coherent state (b) squeezing of vacuum state, and (c) rotation of coherent state.

Displacement

The displacement transformation $D(\alpha)$ is defined as the unitary transformation

$$D(\alpha) = e^{\alpha \hat{a}^\dagger - \alpha^* \hat{a}} \quad (3.6)$$

where $\alpha \in \mathbb{C}$. In the Heisenberg picture, the unitary acts on the quadrature operators as

$$\begin{pmatrix} \hat{x}' \\ \hat{p}' \end{pmatrix} = \begin{pmatrix} D^\dagger(\alpha)\hat{x}D(\alpha) \\ D^\dagger(\alpha)\hat{p}D(\alpha) \end{pmatrix} = \begin{pmatrix} \hat{x} + \frac{\text{Re}(\alpha)}{\sqrt{2}} \\ \hat{p} + \frac{\text{Im}(\alpha)}{\sqrt{2}} \end{pmatrix} \quad (3.7)$$

In other words, $D(\alpha)$ displaces the state in phase space by α , see Fig. 3.2 (a). The displacement gate on any mode is achieved by resonantly driving a mode with microwave signal through the coupling capacitor. The resonant drive can be described by adding an additional term to the Hamiltonian in the rotating frame of the drive as

$$\frac{\hat{H}_d}{\hbar} = \epsilon(t)\hat{a}^\dagger + \epsilon^*(t)\hat{a} \quad (3.8)$$

where $\epsilon(t)$ is the time dependent drive and $\alpha = \int_0^t \epsilon(t')dt'$.

Rotation

The rotation transformation $R(\phi)$ is defined as the unitary transformation

$$R(\phi) = e^{i\phi\hat{a}^\dagger\hat{a}} \quad (3.9)$$

where $\phi \in [0, 2\pi]$. The rotation gate acts to rotate a state in phase space by ϕ about the origin, see Fig. 3.2 (c).

$$\begin{pmatrix} \hat{x}' \\ \hat{p}' \end{pmatrix} = \begin{pmatrix} R^\dagger(\phi)\hat{x}R(\phi) \\ R^\dagger(\phi)\hat{p}R(\phi) \end{pmatrix} = \begin{pmatrix} \cos \phi & -\sin \phi \\ \sin \phi & \cos \phi \end{pmatrix} \begin{pmatrix} \hat{x} \\ \hat{p} \end{pmatrix} \quad (3.10)$$

$R(\phi)$ can be implemented by using a DC pulse in the fast flux line to detune the frequency of a mode briefly in order to accumulate excess phase or it could be simply implemented by changing the rotating frame. Alternatively, one can also make use of the beamsplitter operation and an ancilla qumode to achieve the desired single mode rotation.

$$BS(\pi/4, \phi)BS(\pi/4, 0) = -R(\phi) \otimes R(-\phi) \quad (3.11)$$

Squeezing

Single mode squeezing $S(\xi)$ is defined as

$$S(\xi) = e^{(\xi^*\hat{a}^2 - \xi\hat{a}^{\dagger 2})/2} \quad (3.12)$$

where $\xi \in \mathbb{C}$. Setting $\xi = r$ where $r \in \mathbb{R}$ for purpose of illustration, we can see the squeezing gate acts on the quadrature operator as

$$\begin{pmatrix} \hat{x}' \\ \hat{p}' \end{pmatrix} = \begin{pmatrix} S^\dagger(r)\hat{x}S(r) \\ S^\dagger(r)\hat{p}S(r) \end{pmatrix} = \begin{pmatrix} e^{-r}\hat{x} \\ e^r\hat{p} \end{pmatrix} \quad (3.13)$$

where for $r > 0$ the p quadrature is amplified by e^r at the expense of x quadrature being de-amplified by e^{-r} . Here the Baker Campbell Hausdorff formula is applied noting the commutation relationship $[r(\hat{a}^{\dagger 2} - \hat{a}^2)/2, \hat{a}] = -r\hat{a}^\dagger$.

Applying the squeezing gate on vacuum states gives the squeezed vacuum state where the fluctuation is squeezed below vacuum for one quadrature at the expense of amplified fluctuation in the other quadrature (see Fig. 3.2 (b)). In the limit of infinite squeezing followed by appropriate displacement, one can achieve the zero position $|0\rangle_x$ and zero momentum eigenstates $|0\rangle_p$ which are used in CV quantum teleportation and CV cluster states. Of course, in practice the amount of squeezing r is finite which inevitably introduces errors into these CV protocols that assume an ideal zero momentum eigenstate.

The single mode squeezing gate is achieved in the parametric cavity by degenerate two-photon SPDC process realized through pumping the SQUID at twice the mode frequency. The interaction picture Hamiltonian with the 2ω pump after rotating-wave approximation (RWA) is

$$\frac{\hat{H}_{int}}{\hbar} = g(e^{i\theta_p}\hat{a}^2 + e^{-i\theta_p}\hat{a}^{\dagger 2}) \quad (3.14)$$

where g is dependent on pump power and the axis of the squeezing is determined by the pump phase θ_p .

Beamsplitter

The beamsplitter transformation is defined as

$$BS(\theta, \phi) = e^{\theta(e^{i\phi}\hat{a}_i^\dagger\hat{a}_j - e^{-i\phi}\hat{a}_i\hat{a}_j^\dagger)} \quad (3.15)$$

where θ determines the beamsplitter transmittivity T and reflectivity R and ϕ introduces a relative phase shift. The beamsplitter gate acts on the mode operators to mix the two modes

$$\begin{pmatrix} BS^\dagger(\theta, \phi)\hat{a}_iBS(\theta, \phi) \\ BS^\dagger(\theta, \phi)\hat{a}_jBS(\theta, \phi) \end{pmatrix} = \begin{pmatrix} \cos \theta & e^{i\phi} \sin \theta \\ -e^{-i\phi} \sin \theta & \cos \theta \end{pmatrix} \begin{pmatrix} \hat{a}_i \\ \hat{a}_j \end{pmatrix} = \begin{pmatrix} T & R \\ -R^* & T \end{pmatrix} \begin{pmatrix} \hat{a}_i \\ \hat{a}_j \end{pmatrix} \quad (3.16)$$

where $T = \cos \theta$, $R = e^{i\phi} \sin \theta$ and $|T|^2 + |R|^2 = 1$.

The beamsplitter gate is achieved by pumping the SQUID at the difference of two modes frequencies $\omega_p = |\omega_i - \omega_j|$ which gives the following interaction Hamiltonian after RWA

$$\frac{\hat{H}_{int}}{\hbar} = g(e^{i\theta_p} \hat{a}_i^\dagger \hat{a}_j + e^{-i\theta_p} \hat{a}_i \hat{a}_j^\dagger) \quad (3.17)$$

where the interaction strength g is dependent on pump power and relative phase ϕ is determined by the pump phase θ_p . θ is then the product of interaction strength and the duration of interaction.

Two-mode squeezing

Two mode squeezing is defined by the unitary operator

$$S_2(z) = e^{(z\hat{a}_i^\dagger \hat{a}_j^\dagger - z^* \hat{a}_i \hat{a}_j)/2} \quad (3.18)$$

where $z = r e^{i\phi}$ with r being the squeezing parameter and ϕ being the squeezing angle. In the Heisenberg picture, the operator acts on the bosonic mode operators as

$$\begin{pmatrix} S_2^\dagger(\theta, \phi) \hat{a}_i S_2(\theta, \phi) \\ S_2^\dagger(\theta, \phi) \hat{a}_j^\dagger S_2(\theta, \phi) \end{pmatrix} = \begin{pmatrix} \cosh r & e^{i\phi} \sinh r \\ e^{-i\phi} \sinh r & \cos r \end{pmatrix} \begin{pmatrix} \hat{a}_i \\ \hat{a}_j^\dagger \end{pmatrix}. \quad (3.19)$$

Applying two-mode squeezing to vacuum states, we can get the two-mode squeezed vacuum state also known as the Einstein Podolski-Rosen (EPR) state. This is a commonly used CV entangled state where the modes considered individually are thermal states. However, there exists correlation between the two as seen from squeezing below vacuum in the joint quadratures $\hat{x}_i \pm \hat{x}_j$ and $\hat{p}_i \pm \hat{p}_j$. In the limit of infinite squeezing, the ideal EPR state exhibits perfect correlations between the quadratures of the two modes.

The two-mode squeezing transformation can also model the phase-insensitive amplification process where the signal in one mode is amplified by a gain $G = \cosh^2(r)$ while mixing in noise from the second mode (idler) commonly modeled as a thermal state with average photon number n_{th} .

Two-mode squeezing is achieved by nondegenerate two-photon SPDC through pumping the SQUID at the sum of two mode frequencies $\omega_p = \omega_i + \omega_j$. The process can be visualized

as a pump photon being split into two correlated photons, each in one of the cavity modes. The interaction picture Hamiltonian with the sum frequency pump is

$$\frac{\hat{H}_{int}}{\hbar} = g(e^{i\theta_p}\hat{a}_i^\dagger\hat{a}_j^\dagger + e^{-i\theta_p}\hat{a}_i\hat{a}_j) \quad (3.20)$$

Alternatively, two-mode squeezing may be decomposed into single-mode squeezing and two 50-50 beamsplitter transformation.

$$S_2(z) = BS^\dagger(\pi/4, 0)(S(z) \otimes S(-z))BS(\pi/4, 0) \quad (3.21)$$

3.3.2 Non-Gaussian Resources

We have shown how to implement the basic set of Gaussian transformation and more through driving the cavity or pumping the SQUID. Here we introduce the non-Gaussian resources enabled by the SQUID asymmetry.

Trisqueezed State

A resource state of particular interest is the trisqueezed state defined in [32] as the application of the trisqueezing unitary on the vacuum state

$$|t\rangle = e^{i(t^*\hat{a}^3 + t\hat{a}^{\dagger 3})} |0\rangle \quad (3.22)$$

where t is the triplicity of the trisqueezed state. This state is realized with the degenerate three photon SPDC interaction from pumping the asymmetric SQUID at 3 times the mode frequency $\omega_p = 3\omega$. The interaction Hamiltonian is

$$\frac{\hat{H}_{int}}{\hbar} = g(e^{i\theta_p}\hat{a}^3 + e^{-i\theta_p}\hat{a}^{\dagger 3}) \quad (3.23)$$

where g is dependent on pump strength and θ_p is dependent on pump phase. The Wigner function of an ideal trisqueezed state with triplicity $t = 0.1$ is shown in Fig. 3.3 (a). Non-Gaussianity of the state can be immediately observed from the Wigner function where the distributions has clear dependence on moments of quadratures greater than 2nd order. Further, the negativity in the Wigner function indicates that the state is nonclassical.

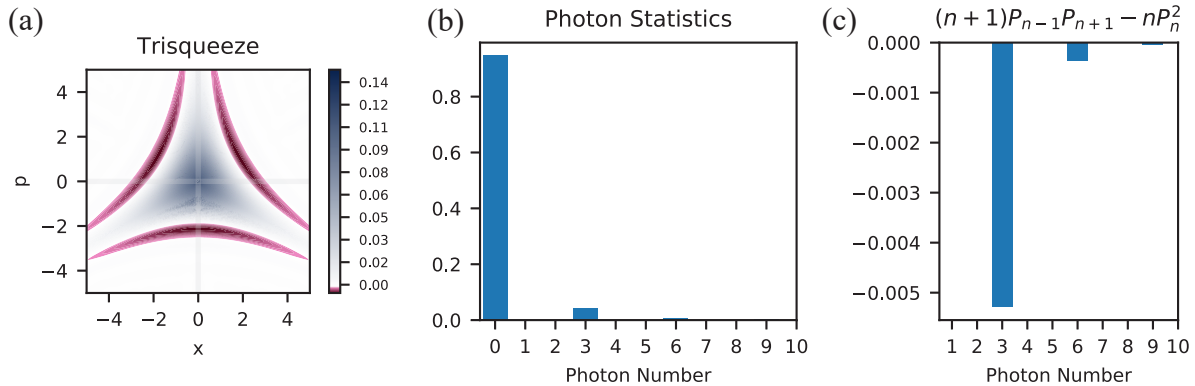


Figure 3.3: Trisqueezed state. (a) Wigner function of an ideal trisqueezed state with $t = 0.1$ where negative regions are highlighted in pink. (b) Photon statistics of this ideal trisqueezed state showing occupation of only Fock states that are multiple of 3. (c) Klyshko’s criterion where a state is nonclassical when $(n + 1)P_{n-1}P_{n+1} - nP_n^2$ is below 0 for any photon number n .

Much like the squeezed vacuum state which consists of only Fock states that are multiple of two, the trisqueezed state only has Fock states that are multiple of three. This can be thought of as a consequence of the three-photon SPDC process always splitting one pump photon into three. Nonclassicality of the trisqueezed state can similar be assessed with the Klyshko’s Criterion whereby a state is nonclassical if $(n + 1)P_{n-1}P_{n+1} - nP_n^2 < 0$ for any photon number n where $n = \{1, 2, 3..\}$ and P_n is photon number probability [33]. The photon number distribution of the ideal trisqueezed state with $t = 0.1$ is shown in Fig. 3.3 (b). The values of $(n + 1)P_{n-1}P_{n+1} - nP_n^2$ are plotted in Fig. 3.3 (c) where we can see that it is below the nonclassicality threshold for any n that is a multiple of three.

Cubic Phase State via Gaussian Conversion Protocol

While the trisqueezed state certainly demonstrates both nonclassicality as well as non-Gaussianity, a preferred choice of non-Gaussian resources used in various CV computation protocols is the cubic phase state. Unlike the trisqueezed state which we already have access to experimentally, the generation of cubic phase state has been elusive so far. However, a recent theoretical proposal by Zheng *et al.* [32] puts forth an exciting protocol that uses only Gaussian transformations to deterministically convert a trisqueezed state into the long sought after cubic phase state. The deterministic conversion protocol involves applying in-line squeezing followed by displacement on the trisqueezed state as shown in

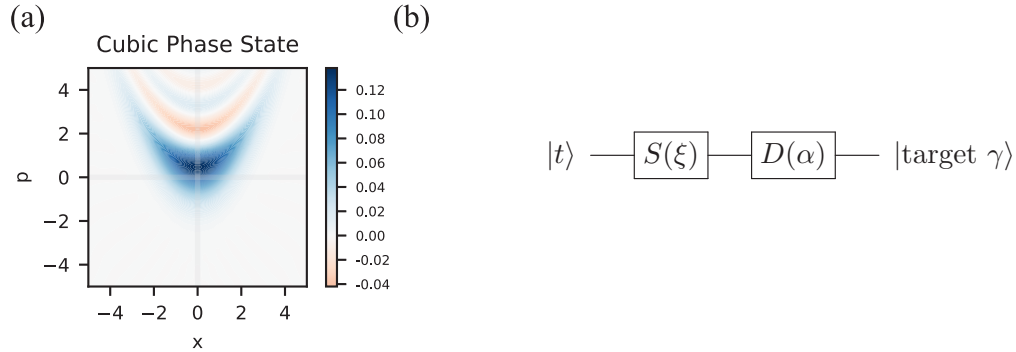


Figure 3.4: Cubic Phase State (a) Wigner function of cubic phase state with 0.5 squeezing and 0.15 cubicity (b) Deterministic protocol to convert a trisqueezed state to cubic phase state [32]

Fig 3.4 (b). This deterministic conversion protocol achieves the cubic phase state with maximum fidelity of 0.971 from input trisqueezed state of $t = 0.1$ [32]. Alternatively, another theoretical proposal from the same group shows one can generate a cubic phase gate directly via simultaneous parametric pumping of the SQUID [34]. Both of these proposals are promising methods to pursue with our device.

3.3.3 Multitone Pumping

Beyond the set of Gaussian gates and non-Gaussian resource state that offers a pathway to the cubic phase state, there are a few other possibly useful transformations involving multitone parametric pumping.

Multimode Entanglement with Multitone Pumping

As mentioned previously, two-mode entanglement can be achieved by two-mode squeezing the initial vacuum states. Chang *et al.* extended the two-mode entanglement process to multimode entanglement using simultaneous parametric interactions. In Ref. [13], Chang *et al.* demonstrated genuine tripartite entanglement in the propagating output state of the parametric cavity by two multitone pumping schemes (see Fig. 3.5). In the coupled-mode (CM) scheme, the SQUID is pumped simultaneously at the sum of first and second mode frequencies $\omega_{p1} = \omega_i + \omega_j$ and at the difference of second and third mode frequencies

$\omega_{p2} = |\omega_j - \omega_k|$. In the bisqueezing (BS) scheme, both pumps are at the sum of the mode frequencies $\omega_{p1} = \omega_i + \omega_j$ and $\omega_{p2} = \omega_j + \omega_k$.

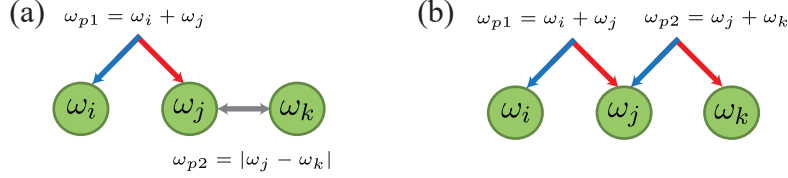


Figure 3.5: Multimode entanglement with simultaneous parametric pumps [13] (a) Coupled-mode (CM) scheme (b) Bisqueezing (BS) scheme

The action of simultaneous pumping is different from if one were to apply the pumps sequentially. For instance, in the CM scheme, the interaction Hamiltonian with the two pump tones under the doubly rotating frame of the pump is

$$\frac{\hat{H}_{int}}{\hbar} = \frac{\hat{H}_S^{ij} + \hat{H}_{BS}^{jk}}{\hbar} = g_1 \left(\hat{a}_i^\dagger \hat{a}_j^\dagger + \hat{a}_i \hat{a}_j \right) + g_2 \left(\hat{a}_j^\dagger \hat{a}_k + \hat{a}_j \hat{a}_k^\dagger \right) \quad (3.24)$$

where the sum frequency pumps between modes i and j introduces the two-mode squeezing term \hat{H}_S^{ij} and difference pump between j and k gives the beamsplitter term \hat{H}_{BS}^{jk} . Time evolution under this Hamiltonian cannot be simply factored into the two-mode squeezing part and beamsplitter coupling part as the two terms do not commute.

$$\left[\hat{H}_S^{ij}, \hat{H}_{BS}^{jk} \right] = g_1 g_2 \left(\hat{a}_i \hat{a}_k - \hat{a}_i^\dagger \hat{a}_k^\dagger \right). \quad (3.25)$$

Despite the two terms not commuting, it turns out the time evolution operator of the CM Hamiltonian can be exactly factored into the following [13]

$$\hat{U}(t) = \exp \left(-i \hat{H}_{int} t / \hbar \right) = \exp \left(-i \hat{H}_S^{ik} t / \hbar \right) \exp \left(-i \hat{H}_S^{ij} t / \hbar \right) \exp \left(-i \hat{H}_{BS}^{jk} t / \hbar \right) \quad (3.26)$$

We see that two-tone pumping results in an additional two-mode squeezing transformation between modes i and k on top of the the expected two-mode squeezing between i and j and beamsplitter transformation between j and k. The additional transformation from simultaneous pumping is responsible for the generation of tripartite entanglement.

While genuine tripartite entanglement was demonstrated in the continuous wave output propagating state of the same parametric cavity device [13], these schemes should be applicable as a gate generating tripartite entangled cavity state which may be a useful resource for computation.

CX and CZ gates

Any two-qumode gate is sufficient to achieve universal CV quantum computation and the beamsplitter transformation is the most commonly used and available one. Nonetheless, there are other two qumode Gaussian gates that may be useful for more efficient implementation of certain algorithms. Controlled-X (CX) and controlled-phase (CZ) gates are two such gates which can also be decomposed into single mode Gaussian gates and beamsplitter gates. CX and CZ gates are defined as the following

$$CX(s) = e^{-is\hat{x}_i \otimes \hat{p}_j / \hbar} \quad (3.27)$$

$$CZ(s) = e^{is\hat{x}_i \otimes \hat{x}_j / \hbar} \quad (3.28)$$

where one can see that the gate couples specific quadrature operators between two modes. $CX(s)$ is also known as the sum gate since the momentum operator is a generator of translation and thus it acts on a state in position basis to add the position in mode i to mode j .

$$CX(s) |x_i, x_j\rangle_{\hat{x}} = |x_i, x_j + sx_i\rangle_{\hat{x}} \quad (3.29)$$

On the other hand, the CZ gate is commonly used as the entangling gate in various protocols such as ones to generate CV Gaussian cluster states.

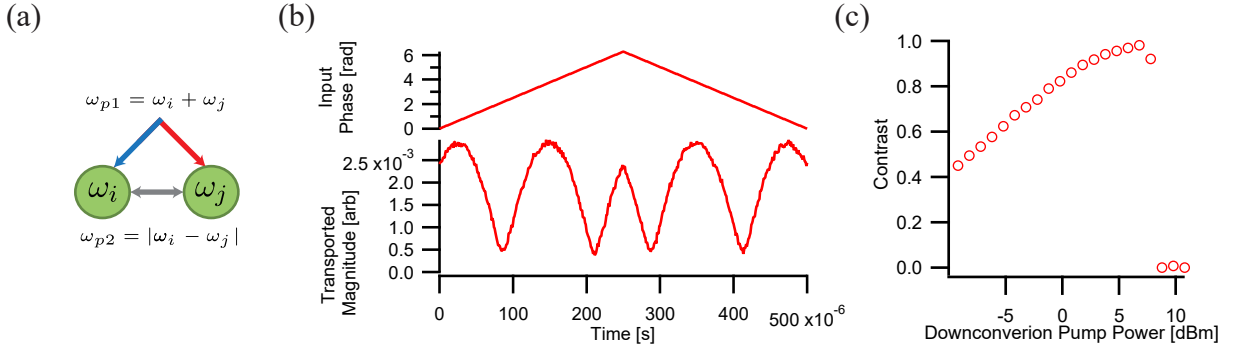


Figure 3.6: Experimental characterization of simultaneous downconversion and beamsplitter pumps (a) Pumping scheme (b) Transport from ω_i to ω_j that is sensitive to input signal phase (c) Contrast of transported quadrature versus suppressed quadrature as a function of downconversion pump power. Unity contrast indicates perfect phase dependent transport at the point of balanced interaction strengths where only one quadrature is transported from input to output mode.

CX and CZ can be implemented in the parametric cavity by two-tone pumping at the sum frequency $\omega_{p1} = \omega_i + \omega_j$ and difference frequency $\omega_{p2} = |\omega_i - \omega_j|$ as shown in Fig. 3.6 (a). The same two-tone parametric pumping scheme has been used recently in a similar architecture to implement a phase-sensitive amplifier with gain-independent bandwidth [35].

The interaction Hamiltonian in the doubly rotating frame of the two pumps consists of both the squeezing term \hat{H}_S and beamsplitter term \hat{H}_{BS} .

$$\frac{\hat{H}_{int}}{\hbar} = \frac{\hat{H}_S + \hat{H}_{BS}}{\hbar} = g \left(e^{i\theta_1} \hat{a}_i^\dagger \hat{a}_j^\dagger + e^{-i\theta_1} \hat{a}_i \hat{a}_j \right) + g \left(e^{-i\theta_2} \hat{a}_i^\dagger \hat{a}_j + e^{i\theta_2} \hat{a}_i \hat{a}_j^\dagger \right) \quad (3.30)$$

where θ_1 and θ_2 are pump phases of the sum and difference frequency pumps respectively. Here the parametric drives are assumed to be balanced such that the interaction strength g are the same for both terms. Experimentally this can be simply achieved by characterizing the device much like a phase-sensitive amplifier in the case of [35] where the phase sensitivity of the frequency converting transport between the modes is dependent on the balance of the parametric drives. Fig. 3.6 (c) shows the phase sensitivity of transport as a function of the downconversion pump power given a set beamsplitter pump power.

Eq. 3.30 can be rewritten into the following

$$\frac{\hat{H}_{int}}{\hbar} = g \left(e^{i\theta_a} \hat{a}_i^\dagger + e^{-i\theta_a} \hat{a}_i \right) \left(e^{i\theta_b} \hat{a}_j^\dagger + e^{-i\theta_b} \hat{a}_j \right) \quad (3.31)$$

where $\theta_a = (\theta_1 - \theta_2)/2$ and $\theta_b = (\theta_1 + \theta_2)/2$. One can see that the sum and difference between the pump phases controls the quadratures from each mode that are coupled together through this interaction. For instance, choosing $\theta_a = 0$ and $\theta_b = \pi/2$, we get the interaction that gives us the $CX(s)$ gate.

3.3.4 Summary of Gate Implementations

Summarized in Table 3.1 are the proposed implementation of various continuous variable gates or resource states. These gates include the basic set of gates necessary to generate the family of all Gaussian transformation (displacement, rotation, single-mode squeezing and beamsplitter) as well as non-Gaussian resource states from three-photon parametric processes.

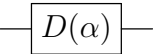
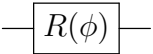
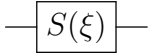
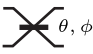
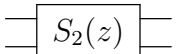
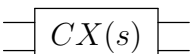
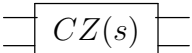
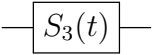
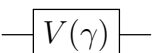
Gate	Symbol	Implementation
Displacement		Resonant drive of cavity modes through the coupling capacitor
Rotation		Change of reference or brief detuning of cavity frequency through flux bias of SQUID
Single-mode Squeezing		Parametric pump at $\omega_p = 2\omega$
Beamsplitter		Parametric pump at $\omega_p = \omega_i - \omega_j $
Two-mode Squeezing		Parametric pump at $\omega_p = \omega_i + \omega_j$
CX		Simultaneous parametric pump at $\omega_{p1} = \omega_i + \omega_j$ and $\omega_{p2} = \omega_i - \omega_j $ with appropriate pump phases
CZ		Simultaneous parametric pump at $\omega_{p1} = \omega_i + \omega_j$ and $\omega_{p2} = \omega_i - \omega_j $ with appropriate pump phases
Trisqueezed		Parametric pump at $\omega_p = 3\omega$
Cubic Phase		Cubic phase state by Gaussian conversion protocol from trisqueezed state [32] or simultaneous parametric pumping scheme [34]

Table 3.1: Summary of CV gates and their proposed implementations in the parametric cavity.

3.4 Measurements

Measurement plays a big role in quantum computation and understanding the type of measurements one can do reliably is especially important. Here we describe the measurement channels and measurements that can be accomplished on the current design as well as potential measurements enabled by minor design modifications.

3.4.1 Cavity Output Mode

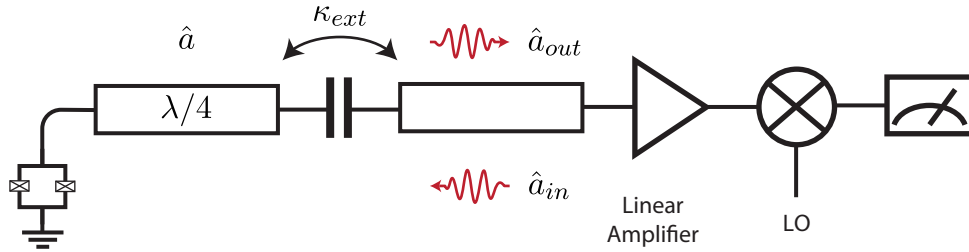


Figure 3.7: Measurement channel of the device. Excitation in the cavity mode is coupled to an output transmission line connecting to a linear amplifier chain leading out of the fridge. At room temperature, the signal is then mixed with local oscillators (LO) and measured.

The primary measurement channel in the device is the capacitively coupled semi-infinite transmission line ideally terminated by a matched load such that device output is not reflected back. The schematic of the measurement setup is shown in Fig. 3.7 where the cavity is connected to transmission line via a partially transmitting boundary condition. The excitation in the cavity decays into the transmission line with a rate of κ_{ext} after which the excitation travels along the transmission line towards the measurement chain consisting of microwave amplifiers, mixers, and finally digitizers that measure the signal.

A semi-infinite lossless transmission line may be modeled as a distributed network of inductors and capacitors that supports the propagation of microwaves. The left \hat{a}_{in} and right \hat{a}_{out} propagating modes are orthogonal but interact with the cavity mode \hat{a} at the coupling point which is described by the input-output relation

$$\hat{a}_{out}(t) = \sqrt{\kappa_{ext}}\hat{a}(t) - \hat{a}_{in}(t) \quad (3.32)$$

\hat{a}_{in} is typically in vacuum state during measurement and \hat{a}_{out} propagates toward the measurement chain where linear measurements like heterodyne or homodyne detection are carried out.

Following the analysis in [36], we can relate the measurement of the output signal sampled continuously in time $\hat{a}_{out}(t)$ to the time independent mode \hat{a} of the cavity at measurement time $t = 0$ by the process of temporal mode matching. The cavity dynamics is described by the following

$$\hat{a}(t) = e^{-\kappa_{ext}t/2}\hat{a}(0) + \sqrt{\kappa_{ext}}e^{-\kappa_{ext}t/2} \int_0^t d\tau e^{\kappa_{ext}\tau/2}\hat{a}_{in}(\tau) \quad (3.33)$$

Integrating the output signal over time with a filter function $f(t)$ gives a time independent mode operator \hat{a}

$$\hat{a} = \int dt f(t)\hat{a}_{out}(t) \quad (3.34)$$

With the choice of an optimal filter function that depends on temporal shape of \hat{a}_{out} as well as properties of coupling between the cavity and transmission line, \hat{a} then corresponds to the cavity mode at the start of the measurement process $\hat{a}(0)$. In this case, the optimal filter function would be one of exponential decay at the rate of κ_{ext}

$$f(t) = \sqrt{\kappa_{ext}}e^{-\kappa_{ext}t/2}H(t) \quad (3.35)$$

where $H(t)$ is the Heaviside function. A non-optimal choice of filter function such as a flat integration window would lead to a reduction in detection efficiency.

3.4.2 Heterodyne Detection

In heterodyne detection, the two quadratures \hat{x} and \hat{p} are measured simultaneously. These two conjugate operators do not commute so the accuracy of the simultaneous measurement is limited by Heisenberg's uncertainty principle. In a typical experimental setup, not only are there significant losses from device output to room temperature instruments, the microwave instruments are also not sensitive enough to detect the low power device output. As such, the signal must first be amplified by a phase insensitive amplifier at cryogenic temperatures. At room temperature, the amplified signal is then mixed with in-phase and out-of-phase local oscillators before sampling with analog-to-digital converters (ADCs) to obtain the two quadrature components.

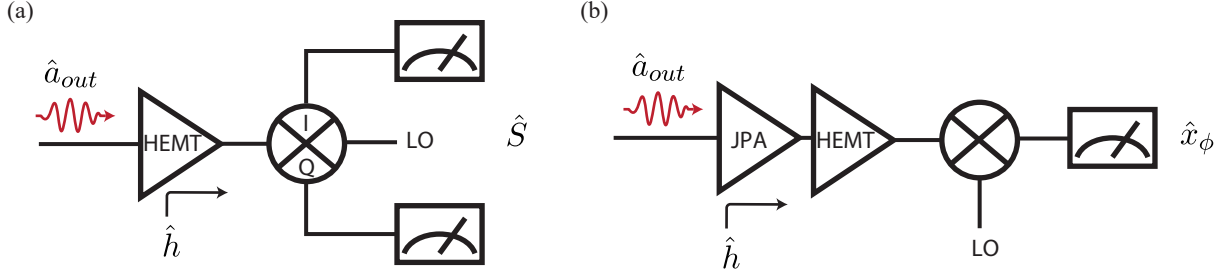


Figure 3.8: Linear measurements. (a) Heterodyne measurement of qumodes involves first amplifying the output state with a phase insensitive linear amplifier chain starting at with a HEMT at 4K stage in our case. The signal is then demodulated with an IQ mixer then the quadratures are measured. (b) Homodyne measurement starts with a phase sensitive amplifier such as a JPA followed by the rest of the amplifier chain. The signal is then mixed with an LO of appropriate phase then measured for the desired quadrature.

In the limit of large gain, this process shown in Fig. 3.8 (a) is modeled as the measurement of the complex amplitude operator \hat{S} that has additional noise mixed in defined as [37]

$$\hat{S} = \sqrt{G}(\hat{x}' + i\hat{p}') = \sqrt{G}(\hat{a} + \hat{h}^\dagger) \quad (3.36)$$

where G is the gain of the phase insensitive amplification and \hat{h} is an ancilla mode to model the noise of the amplification process. Assuming high enough gain for the first amplifier, the noise is dominated by the noise of the first amplifier. With a quantum limited amplifier, such as a Josephson parametric amplifier, the ancilla is in vacuum state and adds the minimum half a photon of noise. In our setup where the first stage of amplifier is a High Electron Mobility Transistor (HEMT) amplifier at the 4K stage, the ancilla is best modeled as a thermal state with average photon number of $n_{th} \approx 25 - 40$ photons.

3.4.3 Homodyne Detection

Homodyne detection is the measurement or projection onto the eigenstates of a single generalized quadrature \hat{x}_ϕ

$$\hat{x}_\phi = \cos(\phi)\hat{x} + \sin(\phi)\hat{p} \quad (3.37)$$

In contrast to heterodyne detection, homodyne detection of a single quadrature can be performed in a noiseless fashion without violating Heisenberg's uncertainty principle. This

measurement can be achieved in our system by using a phase sensitive amplifier as the first stage of amplification for the propagating output mode, see Fig. 3.8 (b). In the ideal case, the amplifier’s action is described by the squeezing transformation along ϕ axis in phase space where the quadrature \hat{x}_ϕ is noiselessly amplified at the expense of its conjugate being deamplified. In practice, perfect measurement efficiency of $\eta = 1$ in noiseless homodyne detection is difficult to achieve especially in microwave regime where the best reported η is only 0.68 [38].

3.4.4 In-Situ Amplification

So far, we have discussed the implementation of common linear measurements on the device output state by the use of linear amplifiers connected to the output transmission line. While state of the art Josephson junction based parametric amplifiers can achieve performance close to the quantum limit in phase insensitive amplification and beyond the quantum limit for phase sensitive amplification, the overall measurement efficiency is typically significantly reduced due the losses from additional required components between the device and the amplifier [39]. This motivates the search for methods to optimize and reduce the losses in the signal path between device and amplifier.

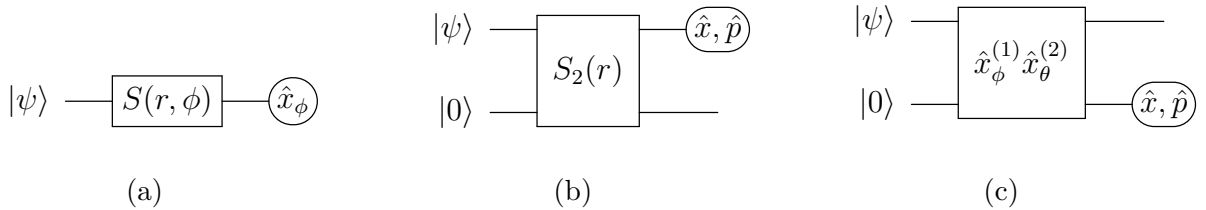


Figure 3.9: Possible schemes for amplification using the same parametric cavity device. (a) Phase sensitive amplification by application of single-mode squeezing. (b) Phase insensitive amplification by application of two-mode squeezing. (c) Phase sensitive amplification with simultaneous beamsplitter and downconversion pumps.

The parametric cavity discussed in this thesis is a device derived from a standard flux pumped JPA and can achieve the same type of parametric interactions as a typical JPA. This presents an interesting opportunity to explore the possibility to use the same device as the first stage of amplification on the cavity modes – allowing us to reduce the impact of losses after device outputs if this in-situ amplification can achieve sufficient gain

and low noise. Some possible in-situ amplification schemes are shown in Fig. 3.9 where single mode, two mode squeezing or two-tone pumping may be used to implement phase sensitive and insensitive amplification. Of course, these proposals are not without flaws. Some immediate concerns may be saturation of device from high signal power or the effect of amplification on other modes of the cavity that all likely have significant undesirable coupling like the cross Kerr due to the SQUID.

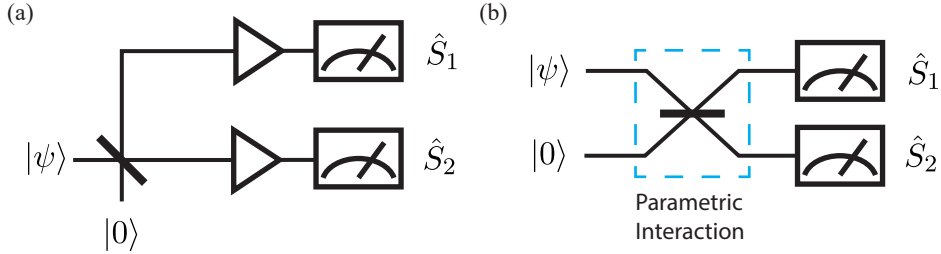


Figure 3.10: Two channel detection for measurement of moments. (a) The detection scheme involves beamsplitting the signal mode with an ancilla mode followed by amplification then heterodyne measurement of both modes. (b) Possible implementation of the measurement scheme using parametric interaction to mix the signal with ancilla mode at different frequency instead of using a physical beamsplitter device.

Another opportunity to make use of the device as part of a measurement chain is the two channel detection setup [40] shown in Fig. 3.10 (a) which can be useful for state tomography. Instead of phase insensitively amplifying then measuring a single complex amplitude operator, the signal mode is first mixed with an ancilla in vacuum then the two output modes \hat{S}_1 and \hat{S}_2 are measured by heterodyne detectors. Under reasonable assumption of ancilla being in vacuum and noise modes of detectors being uncorrelated, the cross-correlations of the two measured complex amplitude operators directly gives the moments of the signal mode which completely describes the state of the mode [40].

$$\langle (\hat{a})^m \hat{a}^n \rangle = \langle (\hat{S}_1^\dagger)^m \hat{S}_2^n \rangle \quad (3.38)$$

Similar experimental setup has been implemented in microwave with the use of transmission line hybrids structure as the beamsplitter [41]; however, these structures are typically designed for narrow bandwidths around a specific frequency. In our device, one can imagine a more flexible implementation where the beamsplitter is a parametric pump pulse between signal and ancilla mode in the same cavity, see Fig. 3.10 (b). The output states are now frequency instead of spatially separated and can be amplified by the same broadband linear amplifier.

3.4.5 Fast Measurement of Cavity State

Thus far, we have discussed linear measurements of cavity modes via the amplification and measurement of the output state in the coupled transmission line. As mentioned in section 2.3, the design is optimal when the cavity is overcoupled to the output transmission line as we don't lose information to channels that are not measured. This presents a trade-off between measurement integration time and cavity lifetime as both are dependent on the same coupling rate to the output transmission line. This is especially an issue for algorithms where additional gates need to be applied after a measurement is completed, such as quantum state teleportation shown in Fig. 3.11.

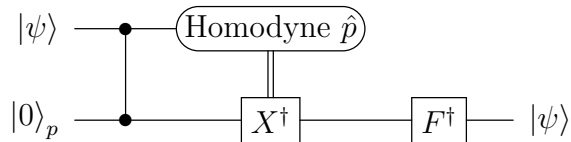


Figure 3.11: Algorithm to realize CV quantum state teleportation. Algorithms like this require application of additional gates dependent on measurement results. As such, it is necessary to have measurements that are magnitudes faster than cavity lifetime.

To address the need to have measurement that is faster than the qumode lifetime, we can employ the same method used in [42] to parametrically convert cavity state to propagating state three order of magnitude faster than the cavity lifetime. The mechanism involves a much lower Q ancilla mode with high coupling rate κ_{out} to the output transmission line. Beamsplitter coupling with coupling $g \ll \kappa_{out}$ converts the state of the high Q mode to the low Q mode which then quickly decays into the output line. In a multimode transmission line resonator, the external coupling naturally increases for higher harmonics as the same coupling capacitor has less impedance at higher frequency. In the current device, a coupling rate ratio of around 8 is already achievable between the 4 GHz mode ($\kappa/2\pi \approx 0.5$ MHz) and 10 GHz mode ($\kappa/2\pi \approx 4$ MHz). The more strongly coupled 10 GHz mode can serve as the readout ancilla mode for the higher Q 4 GHz mode used in computation.

3.4.6 Photon Counting

Photon counting measurement is a useful common component in many CV protocols including Gaussian Boson Sampling. Photon counting involves projecting the state to the

Fock basis with the measurement operators

$$E_n = |n\rangle \langle n| \quad (3.39)$$

In optics, relatively high efficiency photon counting measurement up to tens of photons can be easily achieved with various photon counting detectors like the avalanche photodiode. In microwaves, photon counting especially on a propagating state has been more difficult to do well in part due to the much lower energy of single microwave photon. Nonetheless, in recent years there has been many demonstration and proposals for various photon counters of propagating states typically based on qubits [43] and Joseph junction metamaterial [44]. Integrating these detectors in the measurement chain will enable us to achieve photon counting measurement on the qumodes.

Alternative and likely more efficiently, instead of counting the photons of the propagating output state, we can directly measure the photon number in a cavity with a dispersively coupled qubit. In the dispersive limit where the qubit $\hat{\sigma}_z$ is far detuned in frequency but strongly coupled to the resonator $\hat{a}^\dagger \hat{a}$ the hamiltonian of the system is approximated to be

$$\frac{\hat{H}}{\hbar} = \omega_r \hat{a}^\dagger \hat{a} + \frac{\tilde{\omega}_q}{2} \hat{\sigma}_z + \chi \hat{a}^\dagger \hat{a} \hat{\sigma}_z \quad (3.40)$$

where χ is the dispersive shift that can be seen as qubit state dependent shift of resonator frequency or resonator photon number depend shift of qubit frequency. Naively, to resolve the photon number of the resonator one can just drive with π -pulse and readout the qubit at each of the possible photon number dependent qubit frequency $\tilde{\omega}_q + n\chi$. More efficiently, one can use a Ramsey-like measurement and fast feedforward control to sequentially determine each bit of the photon number in base-2 [43], or synthesize control pulses consisted of arbitrary drive of both qubit and resonator to determine bits of photon number in base-2 [45].

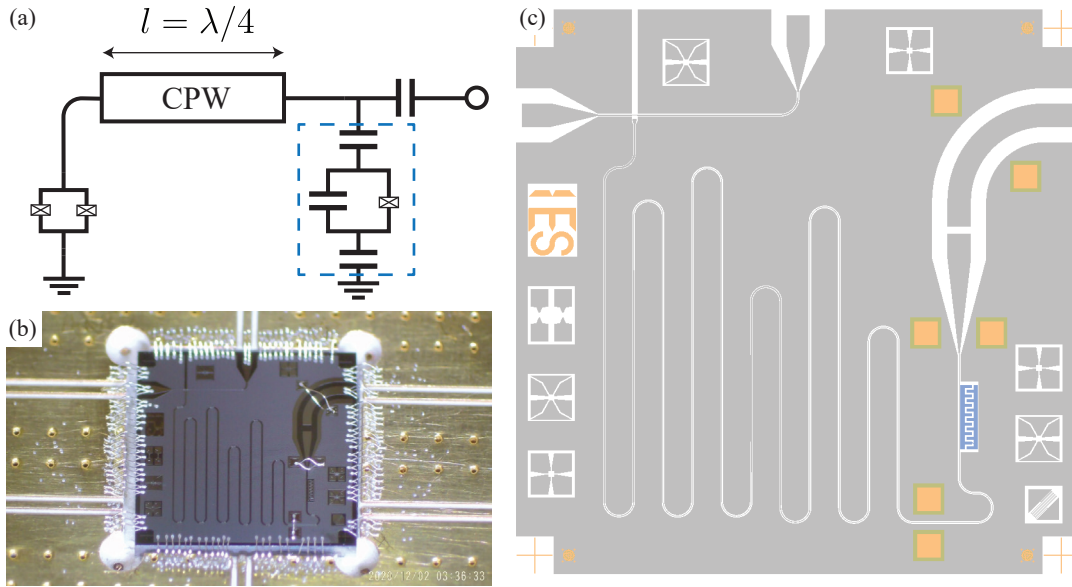


Figure 3.12: Device with qubit probe. (a) A transmon qubit is capacitively coupled to the voltage antinode of the cavity near the coupling capacitor. The qubit frequency and coupling strengths are chosen such that it is dispersively coupled to several modes within our measurement band – allowing us to use it as a nonlinear measurement device of the cavity states. (b) A photograph of the fabricated device. (c) The modified device design where the additional transmon is shown in blue.

f_q	E_C/h	E_J/h	g_{1q}	χ_{1q}	g_{2q}	χ_{2q}
5.2 GHz	253 MHz	14.686 GHz	146.3 MHz	-21.6 MHz	214.75 MHz	47.06 MHz

Table 3.2: Device parameters for a transmon qubit coupled to the parametric cavity

Fig. 3.12 shows the design and layout of a device currently being fabricated to enable some form of photon number related measurement. In this device, a single transmon qubit couples capacitively to the resonator at the voltage antinode near the output capacitor so that it is coupled to all cavity modes. The frequency is chosen such that the transmon is sufficiently detuned from all modes of interest. This qubit is expected to be used as a probe for a lower frequency mode (higher Q) and be readout through a higher frequency mode (lower Q) to which it is also dispersively coupled.

Design parameters for the first devices currently being fabricated are shown in Table 3.2. The resonator frequencies are assumed to be $f_1 = 4.21$ GHz and $f_2 = 6.18$ GHz. g_{iq} and

χ_{iq} are the coupling strength and dispersive shift respectively between the i th resonator mode and the qubit. The first device is designed with relatively strong coupling strengths to observe photon number distribution of the trisqueezed state as the initial objective.

Chapter 4

Experimental Implementation of QKS Algorithm

While we work towards the implementation and characterization the CV gates and resource states detailed in Chapter 3, we can start to demonstrate in parallel the capability of this platform as a quantum computation device by implementing interesting algorithms. We start with using the device to experimentally realize the Quantum Kitchen Sinks (QKS) algorithm [31] which is a hybrid quantum-classical machine learning (ML) algorithm meant for noisy intermediate-scale quantum (NISQ) devices.

4.1 Quantum Machine Learning and the Quantum Kitchen Sinks Algorithm

Quantum machine learning (QML) is an emerging field of research in recent years where there has been many exciting developments especially due to the availability of NISQ devices. Out of the various research directions in QML, quantum kernel methods is a class of algorithms that has been receiving especially more attention in terms of proposals and experimental implementation in various platforms [30, 31, 46, 47, 48].

Quantum kernel methods [49] are inspired by the family of classical ML techniques called kernel methods which includes popular ML algorithms like the support vector machine (SVM). Kernel methods are used for pattern recognition tasks such as the classification problem where the ML algorithm learns to separate data into appropriate classes given some set of labeled training data. Kernel methods involves the use of a similarity

function $k(x, x')$ called the kernel that allows the algorithm to operate on the data points in a higher dimensional feature space where separability of the different classes may be clearer. The kernel function between two data points x and x' is defined as

$$k(x, x') = \langle \phi(x), \phi(x') \rangle \quad (4.1)$$

where ϕ is a map of data from the input space to feature space and the kernel is a proper inner product between the data points in the feature space.

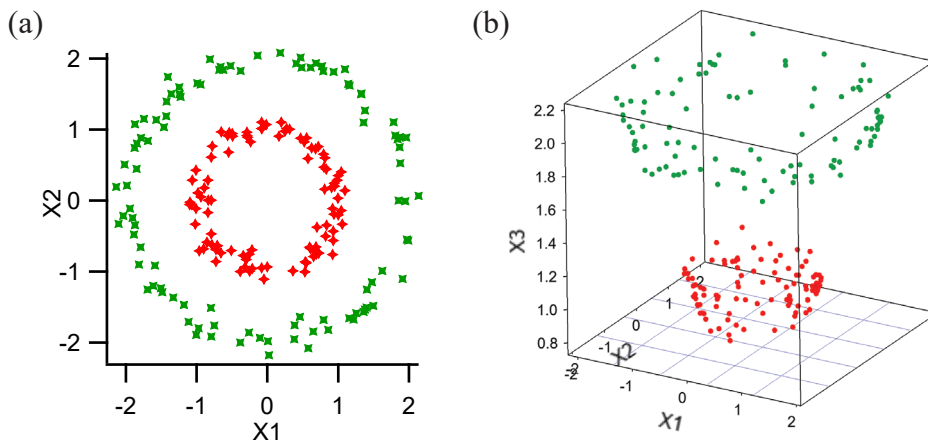


Figure 4.1: (a) Data set containing two classes (red and green) in 2-dimensional input data space. The distributions of concentric circles makes it difficult for linear classifiers to tackle the data set. (b) Data in a higher dimensional feature space become linearly separable.

For instance, Fig. 4.1 shows two classes of data (red and green) in the two dimensional input data space. If one were to use a linear ML algorithm, which learns a linear boundary separating the data classes, it can be seen easily that the classification can never be perfect as the data cannot be separated by a linear boundary. However, imagine the data points in a 3 dimensional feature space with the third dimension being the radius from centre, the data can then be more easily separated even by a linear ML algorithm as one can draw a plane between the two classes.

Quantum kernel methods essentially follow the same logic as classical kernel methods, but seeks to achieve quantum enhancement and perhaps quantum advantage with the use of classically hard kernels implemented in quantum computers. One particular approach is a hybrid one where a quantum computer evaluates a quantum kernel from classical input data then the results are used in a classical ML algorithm to learn the classes. QKS is one such

hybrid algorithm where classical ML techniques are used in tandem with a quantum kernel evaluated on quantum variation circuits. QKS is inspired by a classical kernel method called Random Kitchen Sinks (RKS) [50]. RKS uses many randomized simple nonlinear functions to approximate a kernel in place of the computationally intensive process of optimizing over a complex kernel as one would typically do in other kernel methods like the SVM. In the same spirit, the QKS algorithm is shown in Fig. 4.2 where classical linear random encoding of the data along with the subsequent simple quantum variational circuit are used to implement or approximate a quantum kernel. The result of the quantum circuit is then fed into a classical linear classifier to learn the data classes.

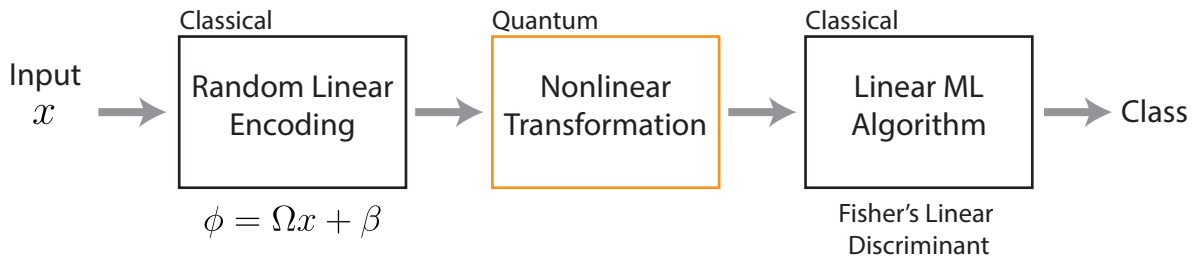


Figure 4.2: Quantum Kitchen Sinks algorithm. The hybrid quantum-classical algorithm consists of classical random encoding and quantum variation circuit implementing some nonlinear transformation to create the quantum kernel of the algorithm. The classification is then done by a linear classical ML algorithm on the output.

4.2 Experiment

Here we look to realize the QKS algorithm experimentally with the quantum part being implemented with the superconducting parametric cavity.

4.2.1 Quantum Variational Circuit with the Parametric Cavity

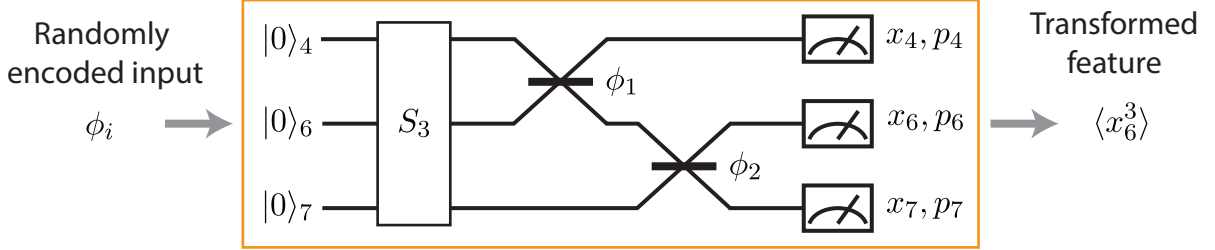


Figure 4.3: The quantum variational circuit implemented in the parametric cavity with two parameters ϕ_1 and ϕ_2 . The circuit starts with 3-photon downconversion to create a non-Gaussian resource state which is then mixed with two beamsplitter gates.

A core component of the QKS is the quantum variational circuit that realizes some nonlinear transformation of the data with a quantum system. The quantum variational circuit implemented is shown in Fig. 4.3. Starting with all modes in vacuum, a pump at the sum of three mode frequencies (4 GHz, 6 GHz, and 7 GHz) first realizes nondegenerate 3-photon SPDC – creating a non-Gaussian resource state which is a necessary condition for potentially classically intractable kernel. The three modes are then mixed with two beamsplitter gates where the phases of the beamsplitters are the parameters of this variational circuit. Finally, a measurement of this quantum variational circuit such as the skew of a quadrature $\langle \hat{x}^3 \rangle$ is taken as the output.

4.2.2 Classical Components of QKS

The quantum variation circuit is only one part of the hybrid algorithm. The relevant classical components includes random linear encoding of the input data as well as a classical ML algorithm. Random linear encoding of the input data x has the form

$$\phi = \Omega x + \beta \quad (4.2)$$

where x is a vector in the input data space. Ω and β are matrices of random variables that are sampled once throughout the algorithm. Ω has a normal distribution with standard deviation σ and mean 0 while the offset β is uniformly distributed from 0 to 2π .

$$\Omega \sim N(0, \sigma^2) \quad (4.3)$$

$$\beta \sim U(0, 2\pi) \quad (4.4)$$

The encoding is done such that for each data point, we get a number of encoded parameter that matches the number of parameters in the quantum variational circuit.

The other classical component of QKS is the classical ML algorithm taking the output of the quantum variational circuits to learn and classify the data. The algorithm used here is a linear binary classifier called the Fisher linear discriminant. This algorithm essentially takes the labeled training data set and finds the best line of projection such that the data of different classes are best separated in this projection in terms of having furthest separated mean as well as smallest variance among each class [51]. The direction of projection is captured in the weight vector \mathbf{w} which is optimized by maximizing the ratio of separation of means over the total within-class variance when the training data are projected. The optimal \mathbf{w} can be found in closed form as

$$\mathbf{w} \propto \mathbf{S}_W^{-1}(\mathbf{m}_2 - \mathbf{m}_1) \quad (4.5)$$

where \mathbf{m}_1 and \mathbf{m}_2 are mean vectors and \mathbf{S}_W is the total within-class covariance matrix. Unknown data can then be projected along this best line of projection “learned” by the algorithm to reduce the data to a single dimension where a threshold then determines the data’s membership to a certain class. See Fig. 4.4.

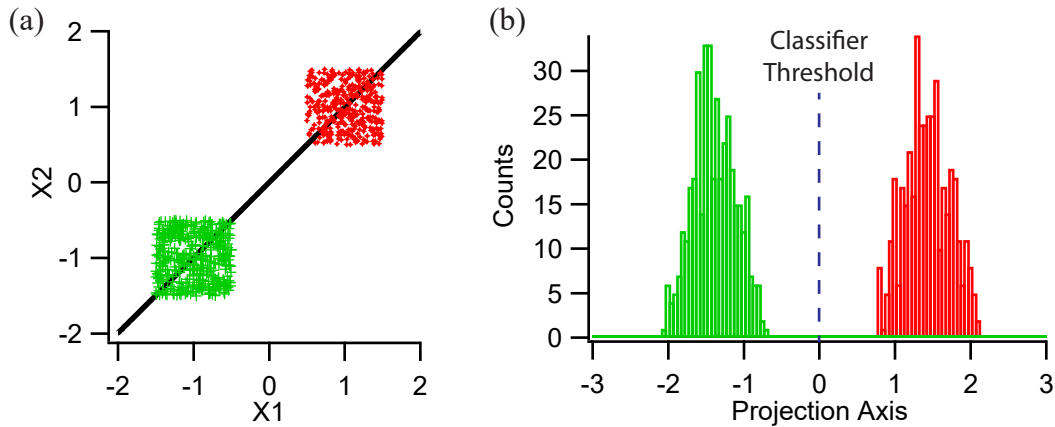


Figure 4.4: An example of Fisher linear discriminant method applied the two classes of data as shown in (a). The ML algorithm learns the projection line as shown in (a) which best separates the projected training data as shown in (b).

4.2.3 Experiment Setup

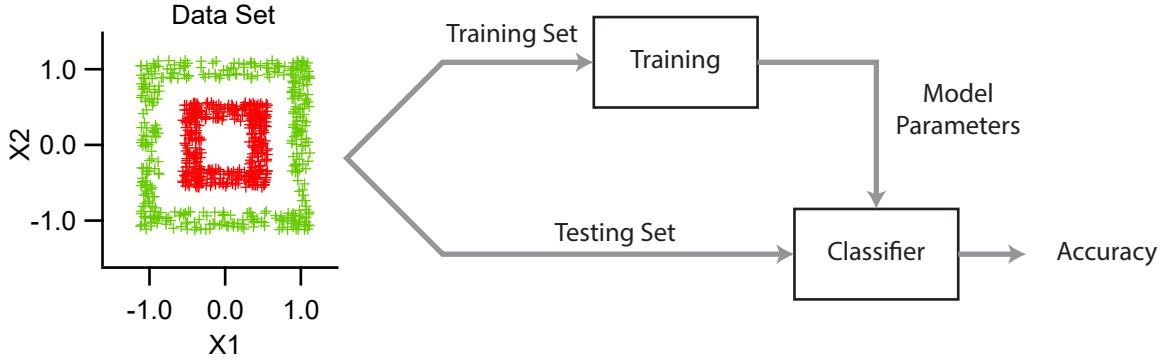


Figure 4.5: Overview of the experiment. Training and testing sets of data are first sampled from the concentric square data set. Training set is used to train the QKS algorithm. Testing set is then used to test the trained classifier to benchmark the performance in terms of classification accuracy.

The experiment carried out is summarized in Fig. 4.5. We start first with a synthetic data set in two dimensions containing two classes (red and green) where the data are drawn from uniform distributions over two concentric squares. This synthetic data set is chosen to benchmark the algorithm as it is a difficult data set to tackle for linear classifiers since it is clear that the data cannot be separated by a simple linear boundary.

A labeled training set of data is first sampled from the distributions then used in the algorithm to build the classifier for the data set. The accuracy of the classifier is then measured by testing the classifier with a testing set of data sampled from the same distributions but have not yet been seen by the algorithm.

In machine learning, there are the so-called hyper-parameters which are higher-level parameters that controls the learning process as opposed to parameters which are “trained” as a part of the learning. We characterize the performance of the algorithm as a function of the two relevant hyper-parameters in our system: σ and the number of episodes. σ is the standard deviation controlling the distribution used in random linear encoding of data. The number of episodes refers to the dimensionality feature space after the data goes through the quantum transformation. Ideally, one would increase the dimensionality and complexity of the quantum transformation by implementing a quantum variational circuit involving more qumodes. However, with the limited size and depth of NISQ devices, we

can increase the dimensionality of the feature space by repeating the same small quantum variational circuit with different sets of random encoding parameters.

The measurement setup for implementation of the quantum variational circuit in the superconducting parametric cavity is shown in Fig. 4.6. The device is cooled down to 7 mK in the dilution refrigerator and we have the output of the cavity connected to an amplifier chain which starts with a HEMT amplifier at 4K. The device is connected to a coil through which we tune the DC flux and parametric modulation of the SQUID is accomplished through a fast flux line with the other end terminated by a 50Ω thermalized to the mixing chamber. Heterodyne measurement of the amplified output signal is done at room temperature using the Aeroflex digitizer which measures the quadratures by I/Q demodulating then digitizing the signal.

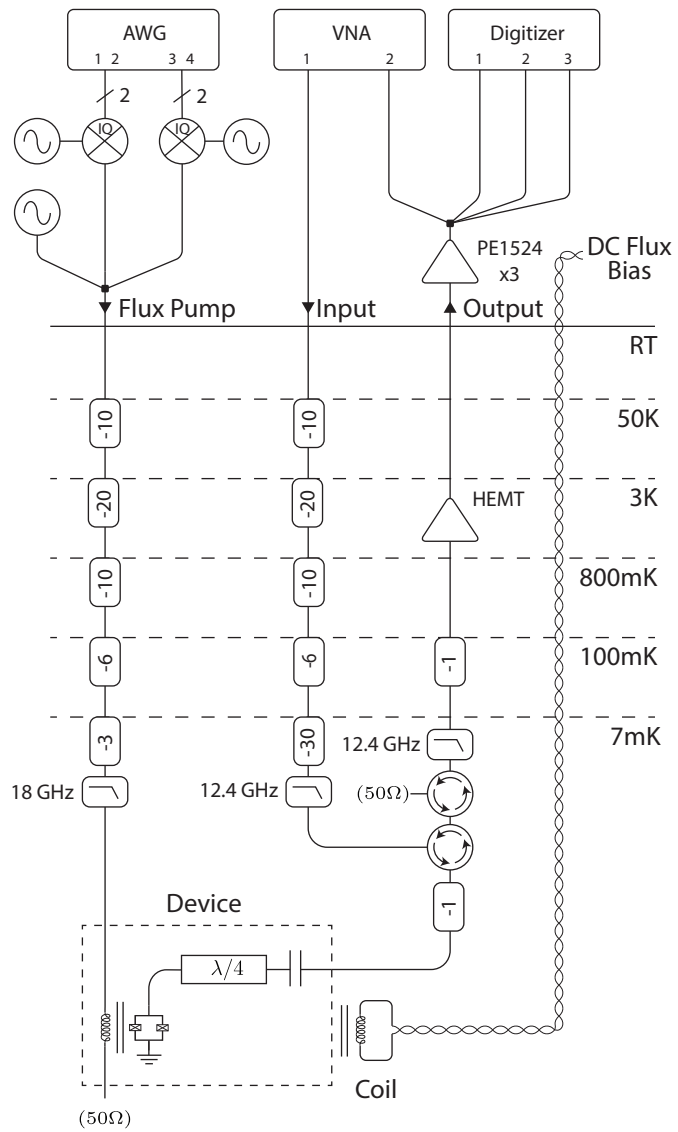


Figure 4.6: Room temperature and cryogenic microwave setup for the experiment.

4.2.4 Mixed Experiment/Simulation

As we work towards implementing control and measurement electronics for pulsed experiments, QKS is first implemented in a mixed experiment/simulation fashion where parts of the quantum variational circuit is simulated in the classical computer.

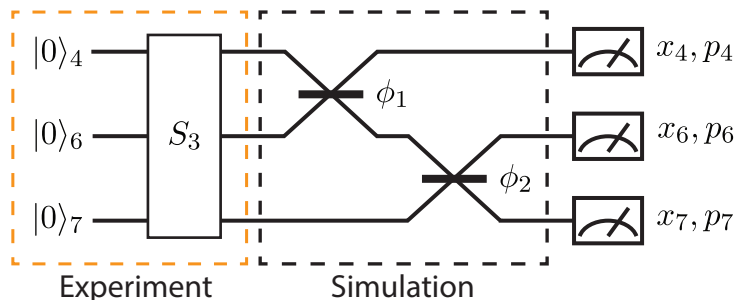


Figure 4.7: Experimental (in orange) time series record of the steady state output under 3-photon downconversion is mixed by digitally simulated beamsplitter gates (in black).

In this scheme as illustrated in Fig. 4.7, the parametric cavity is pumped with a continuous wave (CW) tone at the sum of three mode frequencies to generate a non-Gaussian output state. The steady state output is amplified then its quadratures are measured and stored as classical time series records. Beamsplitter operations between modes are then simulated by digitally mixing the signals. Finally, the skew of one of the quadrature $\langle \hat{x}^3 \rangle$ is taken as the output.

Note in this case where we have CW steady state output, instead of using temporal mode matching to relate the output to the cavity state, we can instead make a discrete mode approximation which allow us to relate the statistics of the output signal to the moments of the cavity state quadrature operators with some factors depending on gain and bandwidth of the measurement [12]. Though in our case, the absolute scaling of the measurement is of no concern as the algorithm is insensitive to constant scaling factor.

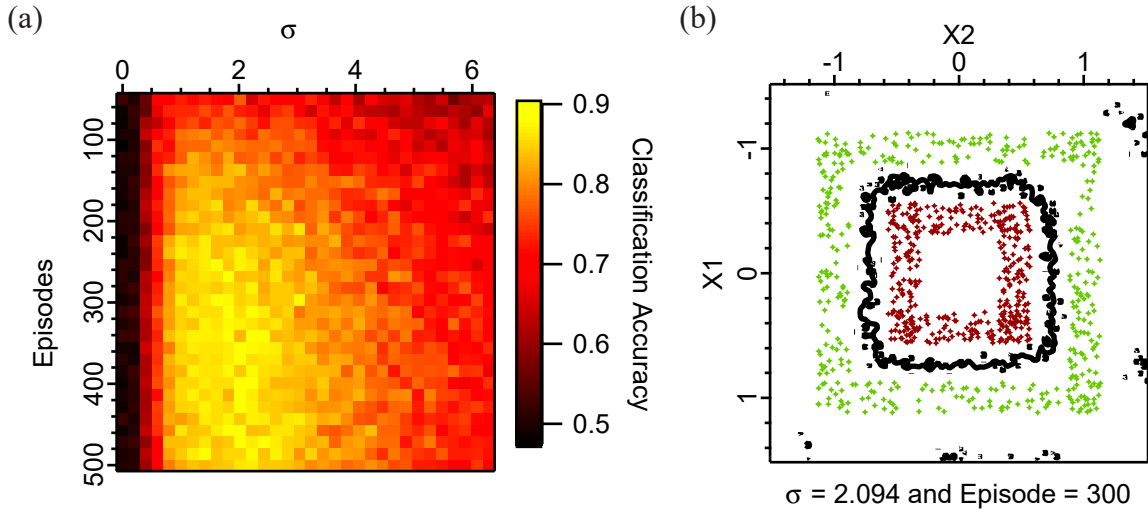


Figure 4.8: Results of the mixed experiment/simulation case (a) classification accuracy of test data as a function of hyperparameters (b) visualization of the classifier by looking at the decision boundary for a specific hyperparameter configuration of $\sigma = 2.094$ and Episode = 300.

Classification accuracy of test data as a function of hyperparameters σ and episodes is shown in Fig. 4.8 (a). It can be observed that in certain regions of the hyperparameter space, the algorithm with the quantum part implemented in the parametric cavity can achieve a classification accuracy up to 90.1% – an improvement over the $50.29 \pm 1.23\%$ accuracy when using only the linear classifier.

Successful classification can further be visualized by the use of the decision boundary representing how the classifier built by QKS divides the input data space into regions for each class. The optimal decision boundary would be one that best separates the two classes in input data space, which in this case should be a concentric square with width right in between the two square distributions. To draw the decision boundary shown in Fig. 4.8 (b), the classifier output is measured throughout the input data space and the contour at 0 which is the threshold between two classes is then the decision boundary. As one can see, with the help of the quantum addition, purely linear classical machine learning algorithm can successfully learn a nonlinear (square) decision boundary to best separate this data set.

4.2.5 CW Pump Experiment

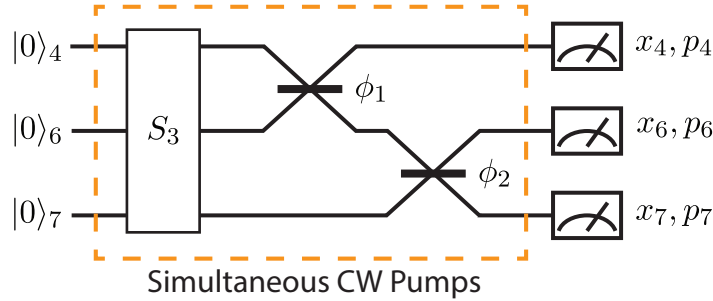


Figure 4.9: The quantum variational circuit is implemented fully experimentally with the device in the dilution refrigerator. Simultaneous CW pumps activating the three interactions of interest are applied in 1ms windows during which the statistics are calculated from heterodyne measurement of the steady state output.

For the next part of the experiment, we implemented the quantum variational circuits fully experimentally in the parametric cavity using simultaneous CW pumps (see Fig. 4.9). The phases of the beamsplitter pump tones are modulated according to encoded data using an IQ mixer and arbitrary waveform generators. For each measurement of the quantum variational circuit, we used an integration window of 1 ms during which we sample the steady state output of the cavity with sampling frequency of 1 MHz.

The classification accuracy as well as decision boundary of at a specific hyperparameter setting are shown in Fig. 4.10. In some region of the hyperparameter space, the algorithm with fully experimental quantum variational circuit can achieve successful classification of the data up to 99.5% accuracy. CW pump experiment achieved a higher classification accuracy due to the better measurement signal-to-noise ratio from a longer integration window. In addition, the mixing of the three modes are done before measurement noise is added which further improves the classification accuracy. Due to the long experimental time required for each configuration of hyperparameters, the CW pump experiment have much lower resolution than the mixed experiment/simulation case. Nonetheless, one can observe general features that agree between the two cases in terms of classification accuracy where the optimal σ is somewhere near $\pi/2$ and optimal episodes is at least 200.

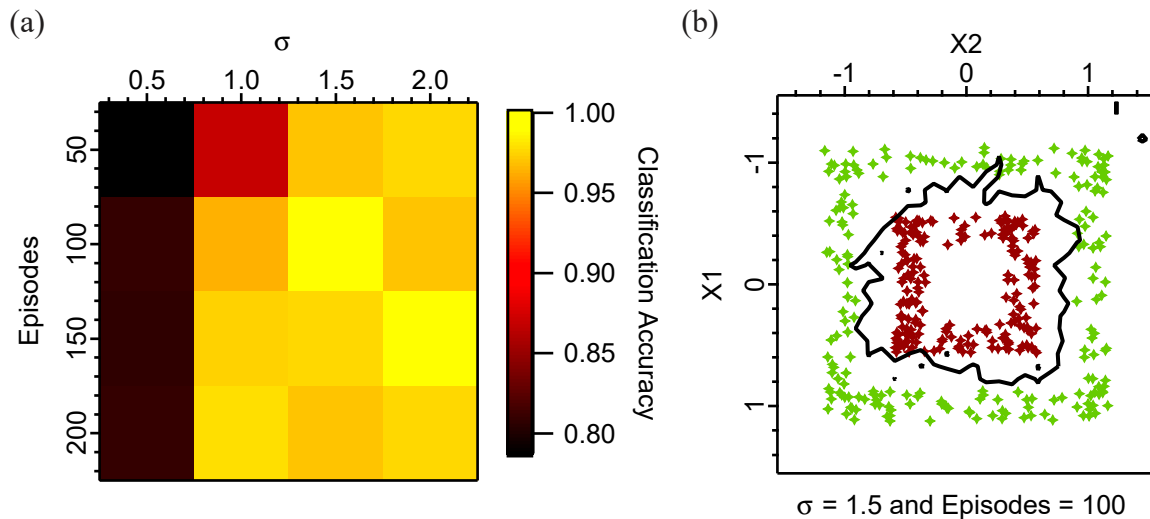


Figure 4.10: Results of CW pump case (a) classification accuracy as a function of hyperparameters (b) visualization of the classifier by looking at the decision boundary for a specific hyperparameter configuration of $\sigma = 1.5$ and Episode = 100.

4.2.6 Summary

In this experiment, we demonstrated the use of the parametric cavity for CV quantum computation by implementing the QKS algorithm experimentally. While we have only tackled a synthetic data set, the experiment shows that the addition of the quantum variational circuit implemented in the parametric cavity is able to realize a significant improvement in classification accuracy in comparison to the baseline case of just a classical linear classifier.

Chapter 5

Conclusion

In chapter 2, the working principle, design and notable features of the superconducting parametric cavity device under study is introduced.

In chapter 3 we present the proposal to realize CV quantum computation using superconducting parametric cavity and provide an overview of the main aspects of computation from gates to measurements. We envision the various harmonics of the parametric cavity being a collection of qumodes and CV gates are successive cavity drive or parametric pump pulses that transform or couple these qumodes. We also discuss the measurement channels and schemes to realize common CV measurements in the current device as well as proposals and new designs which can allow us to achieve other useful measurements on the system.

In chapter 4 we look at demonstrating the capability of the parametric cavity as a computation platform by implementing simple algorithms experimentally. The algorithm of choice is the QKS algorithm which is a hybrid quantum-classical machine learning algorithm that tackles the classification problem. We implemented and benchmarked the performance of QKS in the parametric cavity over two sets of experiments. In the mixed experiment/simulation case, we used available experimental data and digitally simulated beamsplitter operations to realize the quantum part of the algorithm. In the CW pump case, we realize the quantum variational circuit fully experimentally by the use of simultaneous parametric pumps with modulated phase. In both cases, we observed that the quantum part of the algorithm is able to significantly elevate the performance of the linear classifier used in the algorithm – leading to the successful classification of a difficult synthetic data set.

5.1 Future Directions

The work discussed in this thesis is just the start towards the goal of developing a CV quantum computer using the superconducting parametric cavity. The main focus of future work would be to implement various components of the system and characterize them in depth - understanding details such as fidelity of gates and measurement as well as limitation of the architecture. These type of investigations will require efforts from a variety of aspects including the ongoing efforts in scaling up control electronics and improving internal quality factors from fabrication and cryogenic setups.

An especially important near-term goal is the implementation of robust cavity state tomography which will enable us to explore interesting projects such as the characterization of the trisqueezed state, the implementation of the Gaussian conversion protocol for cubic phase state, and another recent proposal in generation of cubic phase state via simultaneous parametric pumping [34]. We have a variety of pathways towards robust tomography and some are as simple as improving our output amplification chain with quantum limited amplifiers to improve noise performance in heterodyne and homodyne detection. Alternatively, we are currently working towards a new device with a coupled qubit as a nonlinear probe to the system which will enable us to directly measure the Wigner function of the cavity state.

Beyond continued efforts in the development of CV quantum computation on cavity states, there are also many interesting research direction in quantum computation using the parametric cavity device. More generally this device can be seen as a flexible platform that provides an extensive toolbox of interactions between the microwave photons confined in the cavity modes. We need not constrain ourselves to the proposed computation scheme that manipulates the cavity state; these interactions can find use in a variety of other computation schemes as well.

One such research direction is the exploration of quantum reservoir computing on this system. Quantum reservoir computing involves the use of a randomly connected quantum network called the reservoir that acts on the input data to this network for a variety of tasks such as the realization of universal quantum computation[52] and machine learning problems [53, 54]. The individually controllable interactions between the multiple bosonic modes in our device makes it a perfect candidate to implement quantum reservoirs. Another direction to explore is the generation of CV cluster state which is the basic resource in measurement-based quantum computation. In an extension to the work on the generation of multipartite entanglement using parametric interactions, there are proposals such as [55] that discusses generation of CV cluster state based on the similar principles.

References

- [1] Pieter Kok, W. J. Munro, Kae Nemoto, T. C. Ralph, Jonathan P. Dowling, and G. J. Milburn. Linear optical quantum computing with photonic qubits. *Reviews of Modern Physics*, 79(1):135–174, January 2007. Publisher: American Physical Society.
- [2] Christian Weedbrook, Stefano Pirandola, Raul Garcia-Patron, Nicolas J. Cerf, Timothy C. Ralph, Jeffrey H. Shapiro, and Seth Lloyd. Gaussian Quantum Information. *Reviews of Modern Physics*, 84(2):621–669, May 2012. arXiv: 1110.3234.
- [3] E. Knill, R. Laflamme, and G. J. Milburn. A scheme for efficient quantum computation with linear optics. *Nature*, 409(6816):46–52, January 2001. Number: 6816 Publisher: Nature Publishing Group.
- [4] Seth Lloyd and Samuel L. Braunstein. Quantum Computation over Continuous Variables. *Physical Review Letters*, 82(8):1784–1787, February 1999. Publisher: American Physical Society.
- [5] Nissim Ofek, Andrei Petrenko, Reinier Heeres, Philip Reinhold, Zaki Leghtas, Brian Vlastakis, Yehan Liu, Luigi Frunzio, S. M. Girvin, L. Jiang, Mazhar Mirrahimi, M. H. Devoret, and R. J. Schoelkopf. Extending the lifetime of a quantum bit with error correction in superconducting circuits. *Nature*, 536(7617):441–445, August 2016. Number: 7617 Publisher: Nature Publishing Group.
- [6] L. Hu, Y. Ma, W. Cai, X. Mu, Y. Xu, W. Wang, Y. Wu, H. Wang, Y. P. Song, C.-L. Zou, S. M. Girvin, L.-M. Duan, and L. Sun. Quantum error correction and universal gate set operation on a binomial bosonic logical qubit. *Nature Physics*, 15(5):503–508, May 2019. Number: 5 Publisher: Nature Publishing Group.
- [7] P. Campagne-Ibarcq, A. Eickbusch, S. Touzard, E. Zalys-Geller, N. E. Frattini, V. V. Sivak, P. Reinhold, S. Puri, S. Shankar, R. J. Schoelkopf, L. Frunzio, M. Mirrahimi,

and M. H. Devoret. Quantum error correction of a qubit encoded in grid states of an oscillator. July 2019.

- [8] Michael Tinkham. *Introduction to Superconductivity*. Courier Corporation, January 2004. Google-Books-ID: VpUk3NfwDIkC.
- [9] B. D. Josephson. The discovery of tunnelling supercurrents. *Reviews of Modern Physics*, 46(2):251–254, April 1974. Publisher: American Physical Society.
- [10] David M. Pozar. *Microwave Engineering, 4th Edition*. Wiley Global Education, November 2011. Google-Books-ID: JegbAAAAQBAJ.
- [11] Alexandre Blais, Arne L. Grimsmo, S. M. Girvin, and Andreas Wallraff. Circuit Quantum Electrodynamics. *arXiv:2005.12667 [quant-ph]*, May 2020. arXiv: 2005.12667.
- [12] Chang, Chung Wai Sandbo. *Two-photon and Three-photon Parametric Interactions in Superconducting Microwave Circuits*. PhD thesis, UWSpace, 2019.
- [13] C. W. Sandbo Chang, M. Simoen, José Aumentado, Carlos Sabín, P. Forn-Díaz, A. M. Vadiraj, Fernando Quijandría, G. Johansson, I. Fuentes, and C. M. Wilson. Generating Multimode Entangled Microwaves with a Superconducting Parametric Cavity. *Physical Review Applied*, 10(4):044019, October 2018. Publisher: American Physical Society.
- [14] C. W. Sandbo Chang, Carlos Sabín, P. Forn-Díaz, Fernando Quijandría, A. M. Vadiraj, I. Nsanzineza, G. Johansson, and C. M. Wilson. Observation of Three-Photon Spontaneous Parametric Down-Conversion in a Superconducting Parametric Cavity. *Physical Review X*, 10(1):011011, January 2020. Publisher: American Physical Society.
- [15] Hadiseh Alaeian, Chung Wai Sandbo Chang, Mehran Vahdani Moghaddam, Christopher M. Wilson, Enrique Solano, and Enrique Rico. Creating lattice gauge potentials in circuit QED: The bosonic Creutz ladder. *Physical Review A*, 99(5):053834, May 2019.
- [16] C. W. Sandbo Chang, A. M. Vadiraj, J. Bourassa, B. Balaji, and C. M. Wilson. Quantum-enhanced noise radar. *Applied Physics Letters*, 114(11):112601, March 2019. Publisher: American Institute of Physics.
- [17] A. Holevo. Some statistical problems for quantum Gaussian states. *IEEE Transactions on Information Theory*, 21(5):533–543, September 1975. Conference Name: IEEE Transactions on Information Theory.

- [18] Stephen D. Bartlett, Barry C. Sanders, Samuel L. Braunstein, and Kae Nemoto. Efficient Classical Simulation of Continuous Variable Quantum Information Processes. *Physical Review Letters*, 88(9):097904, February 2002. Publisher: American Physical Society.
- [19] Michael A. Nielsen and Isaac L. Chuang. *Quantum Computation and Quantum Information: 10th Anniversary Edition*. Cambridge University Press, Cambridge, 2010.
- [20] Arun K. Pati, Samuel L. Braunstein, and Seth Lloyd. Quantum searching with continuous variables. *arXiv:quant-ph/0002082*, June 2000. arXiv: quant-ph/0002082.
- [21] S. L. Braunstein and A. K. Pati, editors. *Quantum Information with Continuous Variables*. Springer Netherlands, 2003.
- [22] Nicolas C. Menicucci, Peter van Loock, Mile Gu, Christian Weedbrook, Timothy C. Ralph, and Michael A. Nielsen. Universal Quantum Computation with Continuous-Variable Cluster States. *Physical Review Letters*, 97(11):110501, September 2006. Publisher: American Physical Society.
- [23] Craig S. Hamilton, Regina Kruse, Linda Sansoni, Sonja Barkhofen, Christine Silberhorn, and Igor Jex. Gaussian Boson Sampling. *Physical Review Letters*, 119(17):170501, October 2017. Publisher: American Physical Society.
- [24] Joonsuk Huh, Gian Giacomo Guerreschi, Borja Peropadre, Jarrod R. McClean, and Alán Aspuru-Guzik. Boson sampling for molecular vibronic spectra. *Nature Photonics*, 9(9):615–620, September 2015. Number: 9 Publisher: Nature Publishing Group.
- [25] Kamil Brádler, Pierre-Luc Dallaire-Demers, Patrick Rebentrost, Daiqin Su, and Christian Weedbrook. Gaussian boson sampling for perfect matchings of arbitrary graphs. *Physical Review A*, 98(3):032310, September 2018. Publisher: American Physical Society.
- [26] Kamil Bradler, Shmuel Friedland, Josh Izaac, Nathan Killoran, and Daiqin Su. Graph isomorphism and Gaussian boson sampling. *arXiv:1810.10644 [math-ph, physics:quant-ph]*, October 2018. arXiv: 1810.10644.
- [27] Maria Schuld, Kamil Brádler, Robert Israel, Daiqin Su, and Brajesh Gupt. Measuring the similarity of graphs with a Gaussian boson sampler. *Physical Review A*, 101(3):032314, March 2020. Publisher: American Physical Society.

- [28] Nathan Killoran, Thomas R. Bromley, Juan Miguel Arrazola, Maria Schuld, Nicolás Quesada, and Seth Lloyd. Continuous-variable quantum neural networks. *Physical Review Research*, 1(3):033063, October 2019. Publisher: American Physical Society.
- [29] Johannes Nokkala, Rodrigo Martínez-Peña, Gian Luca Giorgi, Valentina Parigi, Miguel C. Soriano, and Roberta Zambrini. Gaussian states provide universal and versatile quantum reservoir computing. *arXiv:2006.04821 [quant-ph]*, June 2020. arXiv: 2006.04821.
- [30] Maria Schuld and Nathan Killoran. Quantum Machine Learning in Feature Hilbert Spaces. *Physical Review Letters*, 122(4):040504, February 2019. Publisher: American Physical Society.
- [31] C. M. Wilson, J. S. Otterbach, N. Tezak, R. S. Smith, G. E. Crooks, and M. P. da Silva. Quantum Kitchen Sinks: An algorithm for machine learning on near-term quantum computers. *arXiv:1806.08321 [quant-ph]*, June 2018. arXiv: 1806.08321.
- [32] Yu Zheng, Oliver Hahn, Pascal Stadler, Patric Holmvall, Fernando Quijandría, Alessandro Ferraro, and Giulia Ferrini. Gaussian conversion protocols for cubic phase state generation. *arXiv:2007.03295 [quant-ph]*, July 2020. arXiv: 2007.03295.
- [33] D. N. Klyshko. Observable signs of nonclassical light. *Physics Letters A*, 213(1):7–15, April 1996.
- [34] Timo Hillmann, Fernando Quijandría, Göran Johansson, Alessandro Ferraro, Simone Gasparinetti, and Giulia Ferrini. Universal Gate Set for Continuous-Variable Quantum Computation with Microwave Circuits. *Physical Review Letters*, 125(16):160501, October 2020. Publisher: American Physical Society.
- [35] T.-C. Chien, O. Lanes, C. Liu, X. Cao, P. Lu, S. Motz, G. Liu, D. Pekker, and M. Hatridge. Multiparametric amplification and qubit measurement with a Kerr-free Josephson ring modulator. *Physical Review A*, 101(4):042336, April 2020. Publisher: American Physical Society.
- [36] Christopher Eichler. *Experimental characterization of quantum microwave radiation and its entanglement with a superconducting qubit*. PhD thesis, 2013.
- [37] C. Eichler, D. Bozyigit, C. Lang, L. Steffen, J. Fink, and A. Wallraff. Experimental State Tomography of Itinerant Single Microwave Photons. *Physical Review Letters*, 106(22):220503, June 2011. Publisher: American Physical Society.

- [38] Xiu Gu, Anton Frisk Kockum, Adam Miranowicz, Yu-xi Liu, and Franco Nori. Microwave photonics with superconducting quantum circuits. *Physics Reports*, 718-719:1–102, November 2017.
- [39] F. Lecocq, L. Ranzani, G.A. Peterson, K. Cicak, A. Metelmann, S. Kotler, R.W. Simmonds, J.D. Teufel, and J. Aumentado. Microwave Measurement beyond the Quantum Limit with a Nonreciprocal Amplifier. *Physical Review Applied*, 13(4):044005, April 2020. Publisher: American Physical Society.
- [40] C. Eichler, D. Bozyigit, and A. Wallraff. Characterizing quantum microwave radiation and its entanglement with superconducting qubits using linear detectors. *Physical Review A*, 86(3):032106, September 2012. Publisher: American Physical Society.
- [41] D. Bozyigit, C. Lang, L. Steffen, J. M. Fink, C. Eichler, M. Baur, R. Bianchetti, P.J. Leek, S. Filipp, M. P. da Silva, A. Blais, and A. Wallraff. Antibunching of microwave-frequency photons observed in correlation measurements using linear detectors. *Nature Physics*, 7(2):154–158, February 2011. Number: 2 Publisher: Nature Publishing Group.
- [42] Wolfgang Pfaff, Christopher J. Axline, Luke D. Burkhardt, Uri Vool, Philip Reinhold, Luigi Frunzio, Liang Jiang, Michel H. Devoret, and Robert J. Schoelkopf. Controlled release of multiphoton quantum states from a microwave cavity memory. *Nature Physics*, 13(9):882–887, September 2017. Number: 9 Publisher: Nature Publishing Group.
- [43] Rémy Dassonneville, Réouven Assouly, Théau Peronnin, Pierre Rouchon, and Benjamin Huard. Number-resolved photcounter for propagating microwave mode. *arXiv:2004.05114 [cond-mat, physics:quant-ph]*, April 2020. arXiv: 2004.05114.
- [44] Arne L. Grimsmo, Baptiste Royer, John Mark Kreikebaum, Yufeng Ye, Kevin O’Brien, Irfan Siddiqi, and Alexandre Blais. Quantum metamaterial for nondestructive microwave photon counting. *arXiv:2005.06483 [quant-ph]*, May 2020. arXiv: 2005.06483.
- [45] Christopher S. Wang, Jacob C. Curtis, Brian J. Lester, Yaxing Zhang, Yvonne Y. Gao, Jessica Freeze, Victor S. Batista, Patrick H. Vaccaro, Isaac L. Chuang, Luigi Frunzio, Liang Jiang, S. M. Girvin, and Robert J. Schoelkopf. Efficient Multiphoton Sampling of Molecular Vibronic Spectra on a Superconducting Bosonic Processor. *Physical Review X*, 10(2):021060, June 2020. Publisher: American Physical Society.

- [46] Vojtěch Havlíček, Antonio D. Córcoles, Kristan Temme, Aram W. Harrow, Abhinav Kandala, Jerry M. Chow, and Jay M. Gambetta. Supervised learning with quantum-enhanced feature spaces. *Nature*, 567(7747):209–212, March 2019. Number: 7747 Publisher: Nature Publishing Group.
- [47] Yi Xia, Wei Li, Quntao Zhuang, and Zheshen Zhang. Quantum-enhanced data classification with a variational entangled sensor network. *arXiv:2006.11962 [physics, physics:quant-ph]*, June 2020. arXiv: 2006.11962.
- [48] Moslem Noori, Seyed Shakib Vedaie, Inderpreet Singh, Daniel Crawford, Jaspreet S. Oberoi, Barry C. Sanders, and Ehsan Zahedinejad. Analog-Quantum Feature Mapping for Machine-Learning Applications. *Physical Review Applied*, 14(3):034034, September 2020. Publisher: American Physical Society.
- [49] Riccardo Mengoni and Alessandra Di Pierro. Kernel methods in Quantum Machine Learning. *Quantum Machine Intelligence*, 1(3):65–71, December 2019.
- [50] Ali Rahimi and Benjamin Recht. Weighted Sums of Random Kitchen Sinks: Replacing minimization with randomization in learning. In D. Koller, D. Schuurmans, Y. Bengio, and L. Bottou, editors, *Advances in Neural Information Processing Systems 21*, pages 1313–1320. Curran Associates, Inc., 2009.
- [51] Christopher Bishop. *Pattern Recognition and Machine Learning*. Information Science and Statistics. Springer-Verlag, New York, 2006.
- [52] Sanjib Ghosh, Tanjung Krisnanda, Tomasz Paterek, and Timothy C. H. Liew. Universal quantum reservoir computing. *arXiv:2003.09569 [cond-mat, physics:quant-ph]*, March 2020. arXiv: 2003.09569.
- [53] Aki Kutvonen, Keisuke Fujii, and Takahiro Sagawa. Optimizing a quantum reservoir computer for time series prediction. *Scientific Reports*, 10(1):14687, September 2020. Number: 1 Publisher: Nature Publishing Group.
- [54] L. C. G. Govia, G. J. Ribeill, G. E. Rowlands, H. K. Krovi, and T. A. Ohki. Quantum reservoir computing with a single nonlinear oscillator. *arXiv:2004.14965 [cond-mat, physics:quant-ph]*, April 2020. arXiv: 2004.14965.
- [55] David Edward Bruschi, Carlos Sabín, Pieter Kok, Göran Johansson, Per Delsing, and Ivette Fuentes. Towards universal quantum computation through relativistic motion. *Scientific Reports*, 6(1):1–14, February 2016.